

Contents lists available at [ScienceDirect](https://www.sciencedirect.com)

Medical Image Analysis

journal homepage: www.elsevier.com/locate/media

An automated near-real time computational method for induction and treatment of scar-related ventricular tachycardias

Fernando O. Campos^{a,*}, Aurel Neic^d, Caroline Mendonca Costa^a, John Whitaker^{a,f},
Mark O'Neill^{a,f}, Reza Razavi^a, Christopher A. Rinaldi^{a,f}, Daniel Scherr^e, Steven A. Niederer^a,
Gernot Plank^{b,c,1}, Martin J. Bishop^{a,1}

^a School of Biomedical Engineering and Imaging Sciences, King's College London, London, United Kingdom

^b Gottfried Schatz Research Center Biophysics, Medical University of Graz, Graz, Austria

^c BioTechMed-Graz, Graz, Austria

^d NumeriCor GmbH, Graz, Austria

^e Division of Cardiology, Department of Internal Medicine, Medical University of Graz, Austria

^f Guy's and St. Thomas' NHS Foundation Trust, Cardiovascular Directorate

ARTICLE INFO

Article history:

Received 30 August 2021

Revised 22 April 2022

Accepted 20 May 2022

Available online 27 May 2022

Keywords:

Myocardial infarction
Ventricular tachycardia
Catheter ablation
Computational modeling

ABSTRACT

Catheter ablation is currently the only curative treatment for scar-related ventricular tachycardias (VTs). However, not only are ablation procedures long, with relatively high risk, but success rates are punitively low, with frequent VT recurrence. Personalized *in-silico* approaches have the opportunity to address these limitations. However, state-of-the-art reaction diffusion (R-D) simulations of VT induction and subsequent circuits used for *in-silico* ablation target identification require long execution times, along with vast computational resources, which are incompatible with the clinical workflow. Here, we present the Virtual Induction and Treatment of Arrhythmias (VITA), a novel, rapid and fully automated computational approach that uses reaction-Eikonal methodology to induce VT and identify subsequent ablation targets. The rationale for VITA is based on finding isosurfaces associated with an activation wavefront that splits in the ventricles due to the presence of an isolated isthmus of conduction within the scar; once identified, each isthmus may be assessed for their vulnerability to sustain a reentrant circuit, and the corresponding exit site automatically identified for potential ablation targeting. VITA was tested on a virtual cohort of 7 post-infarcted porcine hearts and the results compared to R-D simulations. Using only a standard desktop machine, VITA could detect all scar-related VTs, simulating activation time maps and ECGs (for clinical comparison) as well as computing ablation targets in 48 minutes. The comparable VTs probed by the R-D simulations took 68.5 hours on 256 cores of high-performance computing infrastructure. The set of lesions computed by VITA was shown to render the ventricular model VT-free. VITA could be used in near real-time as a complementary modality aiding in clinical decision-making in the treatment of post-infarction VTs.

© 2022 The Authors. Published by Elsevier B.V.

This is an open access article under the CC BY license (<http://creativecommons.org/licenses/by/4.0/>)

Abbreviations: AP, Action potential; APD, Action potential duration; AT, Activation time; BZ, Border zone; CARP, Cardiac Arrhythmia Research Package; CV, Conduction velocity; R-D, Reaction diffusion; R-E, Reaction Eikonal; RTT, Round-trip time; V_m , Transmembrane voltage; VT, Ventricular tachycardia; VARP, Virtual-heart Arrhythmia Risk Predictor; VITA, Virtual Induction and Treatment of Arrhythmias.

* Corresponding author at: School of Biomedical Engineering and Imaging Sciences, Rayne Institute, 4th Floor, Lambeth Wing, St. Thomas' Hospital, Westminster Bridge Road, London SE1 7EH, United Kingdom.

E-mail address: fernando.campos@kcl.ac.uk (F.O. Campos).

¹ Joint senior authors.

1. Introduction

Ventricular tachycardia (VT), associated with myocardial infarction, is an important cause of sudden cardiac death (Koplan and Stevenson, 2009; El-Sherif et al., 2017). The only curative treatment for patients with incessant VT is radio-frequency ablation, involving the intense delivery of energy to key targets within the ventricle in order to disrupt the reentrant electrical excitation patterns that sustain the VT (Stevenson, 2013). This highly-invasive therapy is, however, associated with long procedure times and high complication rates, whilst success rates are punitively low; typically > 50% of patients will present with VT recurrence within 1-

year post-procedure (Aliot et al., 2009; Tanawuttiwat et al., 2016; Willems et al., 2020).

Failure of ablation therapy is most often due to an inability to comprehensively identify the myocardial substrate capable of sustaining the VT (Wissner et al., 2012). Attempts to reconstruct the complex intramural propagation pathways through the regions of structural remodelling to identify targets can be limited due to the surface-nature of catheter-based electroanatomical mapping (EAM) systems combined with inadequate spatial resolution (Graham et al., 2017). Furthermore, target identification is most accurate when VT is induced (and mapped) during the procedure which significantly increases the risk-profile and is often not haemodynamically-tolerated, and therefore not feasible (Stevenson, 2009). Importantly, multiple non-clinical VTs are frequently induced in a patient during an ablation procedure, with an inability to induce the arrhythmia responsible for the clinical presentation. Ablation and termination of these induced VTs may have minimal impact on their clinical VT, and is thought to be another key reason behind the high recurrence rate post-ablation.

Recent advances in computational patient-specific modelling have demonstrated the initial feasibility of using *in-silico* image-based models to perform virtual VT induction protocols (Arevalo et al., 2013; 2016), identify reentrant circuits and subsequently target key ablation sites (Chen et al., 2016; Prakosa et al., 2018; Cedilnik et al., 2018). The entirely non-invasive nature of these approaches, requiring only magnetic resonance imaging (MRI) (or computed tomography - CT) imaging data to construct anatomical models, facilitates pre-procedure planning. Furthermore, the ability to apply “aggressive” virtual VT-induction protocols, from numerous sites within the ventricles, allows multiple VTs to be probed, increasing the likelihood of inducing the clinical VT. Once induced, detailed analysis of the ensuing circuits may be performed in conjunction with “simulated ablation” and subsequent re-induction testing, providing the opportunity to directly test target efficacy. Studies using these approaches have demonstrated close association between the geometrical location of *in-silico* ablation target predictions and clinical lesions associated with acute success in both pre-clinical and clinical retrospective studies (Ashikaga et al., 2013; Prakosa et al., 2018; Boyle et al., 2019). In addition, a proof-of-concept prospective study including 5 patients has been performed in which model-based predictions were used to directly guide the ablation procedure (Prakosa et al., 2018). Ablation lesions were created at locations suggested by simulations, with overall successful results. Other studies using similar methods, not focusing directly on ablation, have demonstrated close agreement between personalized model predictions of VT circuits and exit sites with clinically measured VT activation maps during the procedure using both MRI- and CT-based models (Ashikaga et al., 2013; Chen et al., 2016; Deng et al., 2019a).

Undoubtedly, these early successes have paved the way towards *in-silico* personalized model guidance to play a leading role in VT ablation procedures in the (very) near future. However, meeting the full potential of this approach will require its direct integration into clinical workflows, both in terms of time-frames and the requirement for additional (computational) resources. Current approaches largely require vast computational resources to perform monodomain simulations of cardiac electrophysiology (EP) that are costly due to the relatively high-resolution (< 350 μm) meshes required to ensure adequate convergence of numerical solutions, and the long-duration virtual induction protocols that need to be performed to identify all potential circuits. Such requirements necessitate the use of off-site high-performance computing (HPC) infrastructure for simulating (still requiring many hours of compute time) and analyzing the many hundreds of gigabytes of data generated, prior to its use by a clinician (Arevalo et al., 2016; Prakosa et al., 2018).

Eikonal models seek to simulate the spatio-temporal evolution of the wavefront of excitation with the important advantage of maintaining accuracy even when using much coarser computational meshes than required for full monodomain simulations (Colli Franzone et al., 1990; Keener, 1991). The advent of Reaction Eikonal (R-E) approaches offer the potential of combining the advantages of an Eikonal model with the biophysical detail of reaction-diffusion (R-D) approaches, allowing accurate representation of upstroke morphology and repolarization dynamics (Relan et al., 2011; Jacquemet, 2012; Neic et al., 2017; Chen et al., 2016; Cedilnik et al., 2018). The R-E model thus provides an efficient representation of membrane dynamics that can be coupled with full- or pseudo-bidomain models to simulate extracellular potential distributions at a significantly reduced computational cost (Neic et al., 2017). The main current limitation of R-E approaches, however, is their ability to simulate only single, paced beats, *i.e.* a single activation of all nodes within the domain.

In this study, we present an innovative *in-silico* approach that rapidly, and automatically, locates both vulnerable reentry circuits and corresponding ablation targets, in close to real-time using only standard desktop computational resources. We term this non-invasive approach for planning VT ablation VITA (Virtual Induction and Treatment of Arrhythmias). VITA creatively uses R-E infrastructure to identify isolated channels through infarcted regions, assesses their individual vulnerability to form a reentrant circuit, automatically identifies corresponding isthmus exits/entrances, and performs sequential virtual ablation of all target sites to output a minimal (optimal) set of ablation lesions. Following a detailed description of the specific methodological detail underlying our approach, we directly test it against the current gold-standard virtual ablation targeting methodology, quantitatively comparing the VT circuits probed and corresponding computational requirements.

2. Methods

2.1. Computational geometries

Initially, we illustrate the individual steps in VITA using a bi-ventricular geometry of the human heart equipped with an idealized infarct scar. Subsequently, VITA is applied to a virtual cohort of 7 infarcted porcine hearts. Details of the geometrical models are given below.

2.1.1. Idealized model

The bi-ventricular model shown in Fig. 1 was constructed from a whole heart, end diastolic, 3D, steady state free precession cardiovascular magnetic resonance (CMR) with an isotropic resolution of 1.3 mm. Tetrahedral finite elements (FEs) with a mean edge of 976 μm discretization were used to construct the geometrical model (Prassl et al., 2009). In total, 2 459 832 elements and 464 407 nodes make up the computational mesh. Myocardial fiber orientations were incorporated into the model using a rule-based approach (Bayer et al., 2012). Further details about the construction of the anatomical model can be found elsewhere (Crozier et al., 2016). An idealized infarct scar transcended by a network of conducting isthmuses was assigned to the model in order to create pathways capable of sustaining electrical reentries.

2.1.2. Porcine cohort

The virtual cohort of porcine left ventricular (LV) models was built based on late-gadolinium enhanced CMR imaging with an isotropic voxel resolution of 1 mm obtained seven weeks following myocardial infarction (Whitaker et al., 2019). Details of the pipeline used in our group to convert CMR scans into geometrical models of the heart have been reported previously (Campos et al., 2021). Briefly, the LV myocardium and blood pool were manually

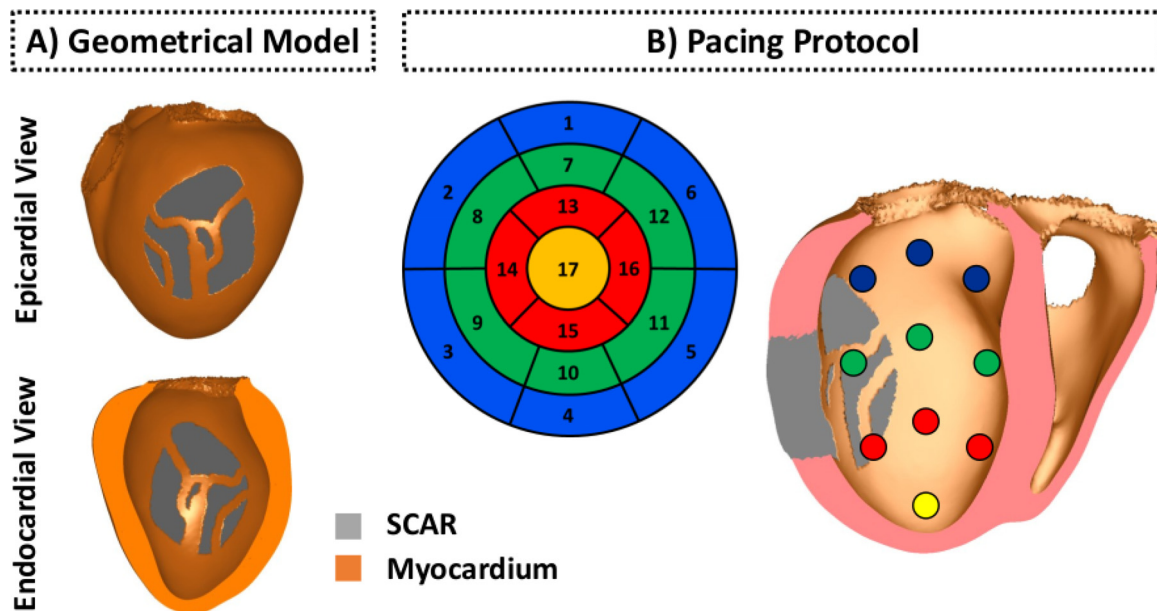


Fig. 1. Idealized human bi-ventricular infarct model. A: Geometrical model of the human heart with an idealized infarct. Myocardial tissue is shown in orange and infarct scar in gray. B: Myocardial wall segments (numbered), as per the American Heart Association nomenclature, and associated pacing sites on the endocardial surface of the left ventricle (right panel).

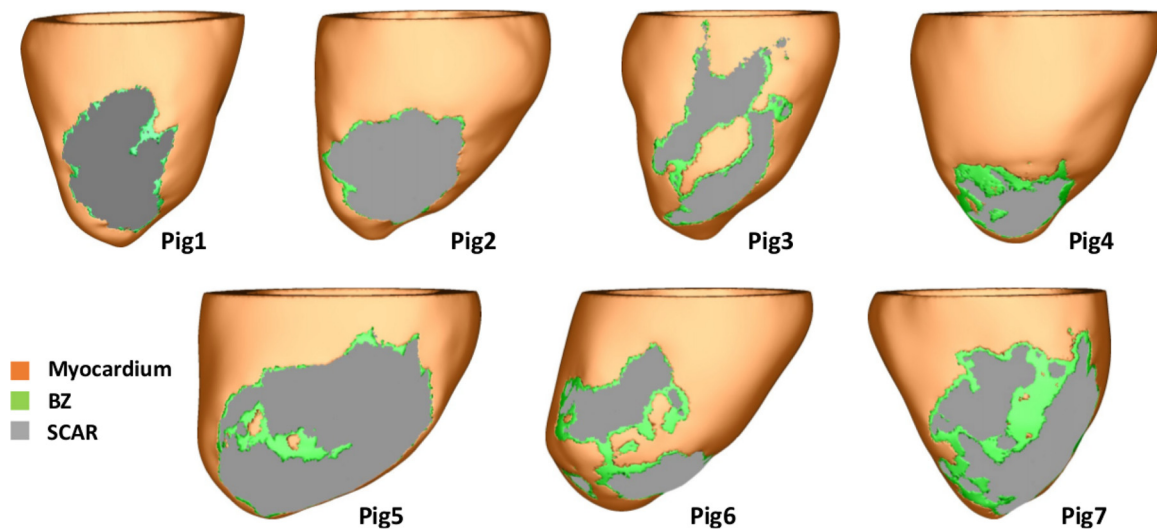


Fig. 2. Cohort of seven porcine left ventricular anatomy models: healthy myocardium (orange), infarct BZ (green), and scar (gray).

segmented by a single observer using Seg3D (www.seg3d.org). The signal intensity range within the segmented myocardium was used to calculate the threshold for scar at 60% of the maximum intensity within the image, and the threshold for the infarct border zone (BZ) tissue at 40% (Perez-David et al., 2011). Tetrahedral FE meshes were created based on the segmented MRI data using custom written software based on the freely available library CGal (Project, 2018). The resulting high resolution models shown in Fig. 2 were discretized with an average FE edge length of 338 μm (Prassl et al., 2009). The meshes in Fig. 2 were down-sampled to 888 μm with Meshtool (Neic et al., 2020) and used to test VITA. As in the idealized model, a rule-based approach was employed to assign fiber orientations within the myocardium (Bayer et al., 2012).

2.2. Eikonal model

Eikonal models sit at the core of VITA as they represent a fast way to simulate the cardiac wavefront of excitation using much

coarser computational meshes (Colli Franzone et al., 1990; Keener, 1991). Activation wavefronts are computed by solving the Eikonal equation:

$$\sqrt{\nabla t_a^T \mathbf{V} \nabla t_a} = 1 \quad \text{in } \Omega \quad (1)$$

$$t_a = t_0 \quad \text{in } \Gamma \quad (2)$$

where t_a is a function describing the wavefront arrival time at location \mathbf{x} , \mathbf{V} is the squared conduction velocity (CV) tensor, which combines with the longitudinal and transversal fiber orientations (l, t) in the myocardium Ω with associated scalar velocities (v_l, v_t). The boundary condition t_0 in Γ represents location and timing of the stimulation initiating activation. CVs of $v_l = 0.50$ m/s and ($v_t = 0.16$ m/s were assigned to the healthy myocardium to reproduce velocities produced by the monodomain equations with the conductivities in Section 2.5. Isotropic CV of 0.16 m/s was assigned to the BZ (porcine cohort only) to represent the effects of fiber dis-

array and presence of fibrosis known to follow myocardial infarction (Mendonca Costa et al., 2018).

For computing distance fields, the Eikonal equation can be simplified by using $v_l = v_t = 1$ and therefore $\mathbf{V} = \mathbf{I}$, the identity matrix, to

$$\|\nabla t_a\| = 1 \quad \text{in } \Omega \quad (3)$$

$$t_a = 0 \quad \text{in } \Gamma \quad (4)$$

where t_a now represents the distance and travel time from Γ to \mathbf{x} .

2.3. Computational environment

All experiments using VITA were performed in coarser geometrical models and carried out on a 12-core Intel(R) Xeon(R) CPU E5-2670 v3 2.30 GHz (64 bit Linux) desktop machine with 64 GB of RAM memory. Biophysically realistic simulations within high resolution models were performed on 4 nodes of our internal HPC cluster machine, with each node consisting of a 64-core (2 sockets, 32 cores/socket) AMD EPYC (64 bit Linux) machine equipped with 256 GB of RAM memory. Execution times are presented as the time each approach required to run on its respective computational environment as well as on a single CPU. CPU times are taken as the execution time on the parallel computing environment multiplied by the total number of cores used to run each approach.

2.4. Rationale of the method

The rationale for the algorithm behind VITA is based on finding isosurfaces associated with a paced activation wavefront that splits within the ventricles due to the presence of isolated isthmuses generated by scar and surviving tissue. Such isthmuses provide isolated conduction pathways that are disconnected from the rest of the myocardium. This rationale is illustrated in Fig. 3.

In the absence of an isolated isthmus, a single connected isosurface exists (blue box); when it encounters the isthmus, the isosurface “splits” into two components (red box), with a smaller isosurface within the isthmus itself, which is unconnected to the larger isosurface wrapping around the rest of the ventricles due to the nonconducting scar at its boundaries. By locating the regions in space at which these isolated isthmuses appear and disappear allows the identification of entry and exit sites, respectively, which could be used to guide ablation to target the required sites within the isthmus.

Once an exit (or entry) site is located, the mesh is split along its respective isosurface to create a local region of unidirectional conduction block. Cardiac activation is then simulated using a fast Eikonal model. Fig. 4 summarizes all steps comprising the VITA approach. The specifics of each step is described in detail as follows.

2.4.1. Split surfaces

First, a distance field is computed from a source point, or stimulus site. The distance field depends on the location of the stimulus and on the anatomy of the 3D scar. Fig. 5A shows distance fields computed from pacing sites located at the LV apex (top panel) and base (bottom panel). Split isosurfaces are determined by mesh connectivity analysis (edge-graph traversal). By comparing relative isosurface size (area of all triangles of the isosurface), the surface fragments are grouped in inside and outside of an isthmus. For each split, the largest isosurface is ignored as this is the one that wraps around the “rest” of the ventricles, outside of the scar. While the algorithm does not know the macroscopic isthmus structure, it assumes that the distance field does not start and does not end in the isthmus. Therefore, there is a sequence of isosurface fragments that sample the isthmus structure, where the isosurfaces

with no downstream neighbors are denoted as “start” and isosurfaces with no upstream neighbors are denoted as “end” of the isthmus structure. If more than two split surfaces are detected, the isosurface fragments are tested individually and also combined. This step aims to account for the presence of fibrosis within the isthmus that would result in many smaller split surfaces. This is necessary as wavefront simulation after disconnecting the mesh only at specific “micro” split surfaces inside the isthmus would result in normal propagation, whereas disconnection of all small isosurfaces would create unidirectional block. In both examples in Fig. 5, isosurfaces are separated by 1 mm (approximately the mean discretization of the geometrical model, see Section 2.1.1). Locations where isosurfaces split within the LV are illustrated in Fig. 5B. While both isosurfaces are seen as lines on the epicardial surface of the LV, they are in fact three-dimensional across the ventricular wall. In total, 70 and 66 split isosurfaces were detected in the apical and basal distance fields, respectively.

2.4.2. Detection of exit sites

Second, amongst all split isosurfaces only those without downstream neighbors are selected. No topology analysis (e.g. splitting and rejoining of conduction paths) is performed on the isosurface fragment sequences. Downstream/upstream neighborhood is determined with a steepest descent/ascent of the distance field along the mesh edge graph. These represent regions where the specific isosurface terminates, by either recombining with a larger isosurface or by annihilation with a wavefront traveling in opposite direction (collision). Such isosurfaces represent distal mouths or the exit sites of channel isthmuses within the scar. Fig. 5B illustrates the detection of two different exit sites in the idealized model after pacing from the apex (top panel) and base (bottom panel). Split surfaces detected within the isthmuses are shown in different colors based on their distances d to the pacing sites. Split surfaces in green are associated with distal mouths, i.e., exit sites (Fig. 5B, inset) as they do not have a downstream neighbor. Split surfaces in red, on the other hand, represent entrances which are regions where the first split was detected (no upstream neighbor). Note that the detected exit sites are not exactly located at the distal mouths of the isthmuses. This is due to collisions of isosurfaces at those regions. Although the detection of only one exit per stimulus site is illustrated in Fig. 5, in total, 3 (out of 70 split surfaces, see Section 2.4.1) and 2 (out of 66 split surfaces) exits were detected when pacing from the apex and base, respectively. Under a given pacing location the exit sites, rather than entrances, were chosen as they are often used to guide catheter ablation therapy of VTs.

2.4.3. Fast VT induction

Once all exit sites for a given distance field are detected, the next step is to check whether they can sustain VTs. This is achieved by simulating unidirectional conduction block at the exit site. Unidirectional block was created by disconnecting the isosurface associated with the detected exit site, creating a region of uncoupled tissue across which activation cannot travel. Isosurface disconnection is done using a discontinuous FE approach that imposes electrical insulation along edges of FEs (Costa et al., 2014). Briefly, elements lying on the isosurface are marked for insulation. Insulation is enforced by decoupling nodes shared between adjacent FEs. Shared nodes are then duplicated, with one set located on one side of the insulating surface while the other set, with same spatial coordinates, is assigned at the opposite side of the isosurface. Cardiac activation is then initiated on a set of nodes on one side of the decoupled surface, automatically ensuring unidirectional block of the wavefront, which propagates along a single direction along the isthmus. Fig. 6 shows activation time (AT) maps of VTs associated with 3 and 2 exit sites detected after pacing the model at the apex (top panel) and base (bottom panel), respectively. Activation

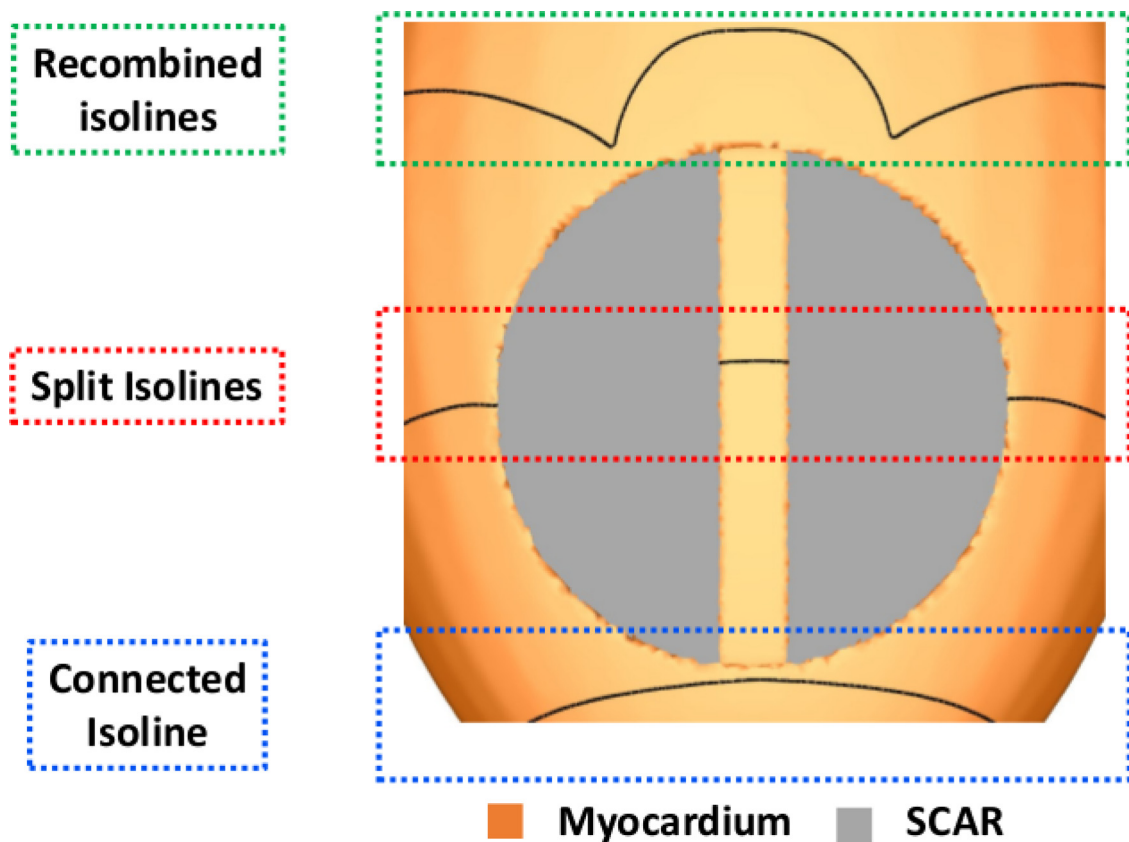


Fig. 3. Splitting of isosurfaces. Isolines illustrating the regions where the wavefront splits due to the presence of an isthmus inside the scar (red box).

was initiated by taking $t_0 = 0$ ms (Eq. 2) at nodes located at the exit site.

The time the wavefront takes to travel back to the region of block, *i.e.* the activation time of the nodes on the distal side of the decoupled surface (see Fig. 6), is referred here as the round-trip time (RTT). RTT is used here as a metric to assess whether the reentrant pathway associated with a detected exit site is long enough to sustain VTs.

2.4.4. Simulating VT dynamics and ECGs

VITA also allows for a quick investigation of electrical wavefront propagation during VT patterns, and associated extracellularly sensed potential fields, either sensed as electrocardiogram (ECG) at the body surface or as electrogram (EGM) by an implanted device. This extra step is achieved by solving a R-E model that uses Eikonal-based activation patterns to compute the distribution of electrical sources (Neic et al., 2017). Unlike R-D models, R-E models are not locked into using high spatial resolutions, and, as such, can be solved quickly, with close to real-time performance. The reaction part of both R-E and R-D models is simulated by solving a computational model of the ventricular action potential (AP) such as the ten Tusscher (TT) model (ten Tusscher and Panfilov, 2006).

The R-E model provides a fast way to obtain EGM and ECG signatures of the VT for clinical comparison. ECGs are obtained by sampling the potential field at lead locations that approximate clinical standard electrode positions. This can be achieved, with high fidelity, using a lead field approach (Potse, 2018; Gillette et al., 2021), or, approximately, by resorting to ϕ_e recovery techniques that make the simplifying assumption of the heart being immersed in a uniform volume conductor of infinite extent (Plonsey and Barr, 1998). Examples of computed ECGs related to the Einthoven limb leads and their associated VTs are shown for one VT cycle in Fig. 7.

R-E and R-D simulations within all models presented here were performed with CARPentry-Pro (Neic et al., 2017) (NumeriCor GmbH, Graz, Austria), built upon openCARP (Plank et al., 2021). Algorithms underlying the R-D model, as implemented in the Cardiac Arrhythmia Research Package (CARP), have been described extensively elsewhere (Vigmond et al., 2008) (<http://carp.medunigraz.at>).

2.4.5. Multi-site pacing

As shown in Fig. 6, different VTs can be induced depending on the distance field, or pacing location in a clinical setting. This suggests that multi-site pacing may be necessary to detect all vulnerable regions. Multi-site pacing was implemented by computing distance fields from the 17 locations on the endocardial surface of the LV shown in Fig. 1B.

In total, 53 VTs were detected by VITA for all 17 pacing locations in the idealized model. All VTs satisfied two conditions: they were associated with an exit site and had a RTT of at least 50 ms. While this value is lower than reported VT cycle lengths (Nishimura et al., 2021), it allowed us to highlight as many circuits as possible, including less likely VTs that may only form under more extreme pathological conditions such as very short AP duration (APD) and very slow conduction within the isthmus network.

2.4.6. Unique VT discrimination

Several VTs induced by the VITA protocol may be similar or even identical. This is illustrated in Fig. 7A, which shows three VTs induced from separate exit sites. In a next step identical or very similar VTs will be reduced to a set of unique VTs. Two approaches were considered. First, VT uniqueness was assessed by computing the correlation coefficient between QRS complexes of

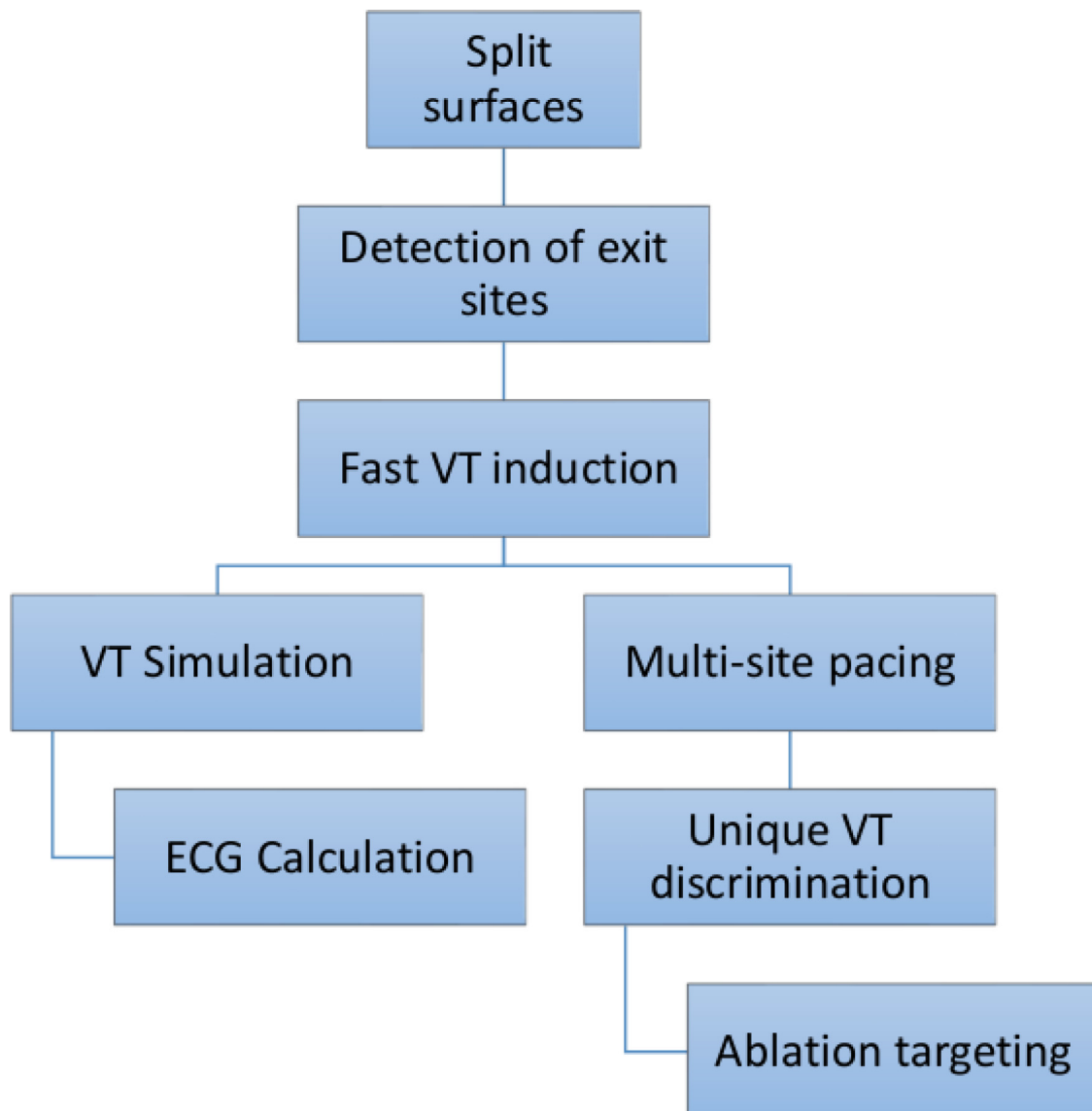


Fig. 4. Conceptual diagram showing the steps of VITA.

the simulated ECG signals linked to a given VT (Fig. 7C). This approach follows EAM procedures where VT circuits are identified by comparing the QRS signature of a VT to a template QRS signature of a previously recorded VT. While this approach offers the potentially significant advantage of comparing QRS signatures to available EGM or ECG signals to ascertain that simulated and observed VT are closely related, the power to robustly discriminate VTs of subtly different reentrant pathways was limited. Thus, secondly, correlation coefficients were also computed between AT maps to assess uniqueness among very similar VTs. For this sake, AT maps were cyclically aligned prior to the correlation calculation based on the RTT, such that they had the same starting location ($t = 0$). The Pearson product-moment was used to compute the correlation coefficient between AT maps of two VTs. Different threshold values for the correlation coefficients were tested for the detection of unique VTs. VTs with a correlation coefficient smaller than (or equal to) the threshold were considered unique, whereas VTs with coefficients larger than that were considered redundant. The threshold of 0.8 was chosen as values above it resulted in redundant VTs. All unique VTs detected by VITA in the idealized model are shown in Fig. 8A.

Note that there are VTs induced from similar exit sites (dashed arrows), but these VTs have opposite chirality and are considered here to be unique (correlation coefficient smaller than the threshold). Also, the exit sites associated with VTs 1 and 2 are located inside the isthmus, rather than at one of the mouths connecting the isthmus to the bulk LV. This is because of 1) distance fields associated with pacing sites located on the opposite side of the heart (in relation to the infarct) led to collisions of isosurfaces within the isthmus. Such isosurfaces were classified as exit sites as they met the criterion of not having downstream neighbors; and 2) the anatomy of the idealized infarct. As can be seen Fig. 8, surviving bundles of myocardium branch and merge within the scar (larger central isthmus). This led to the formation of exit sites near those regions.

2.4.7. Ablation targeting

The last step of VITA is the detection of ablation targets aiming to terminate all VTs. The detection of ablation targets is performed by iterating over the ordered list of exit sites. Starting with the exit site of longest RTT, a unidirectional block is imposed by disconnecting the nodes associated with the exit site as described in

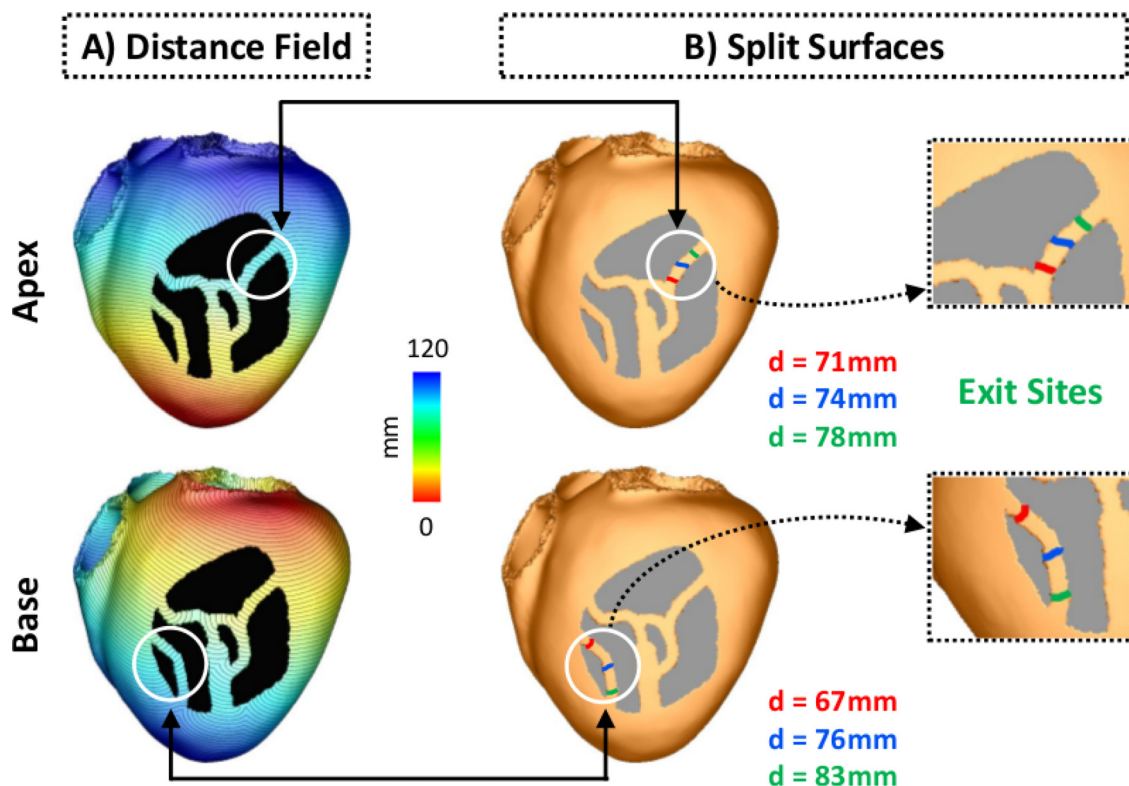


Fig. 5. Detection of exit sites. A: Examples of distance fields computed from pacing sites located at the apex (upper panel) and base (bottom panel). B: Split surfaces detected within the isthmuses at different distances d from the pacing sites. Isosurfaces in green are associated with the distal mouths, i.e., exit sites, of the isthmuses. 3D surfaces are shown as lines on the LV epicardium for visualization purposes.

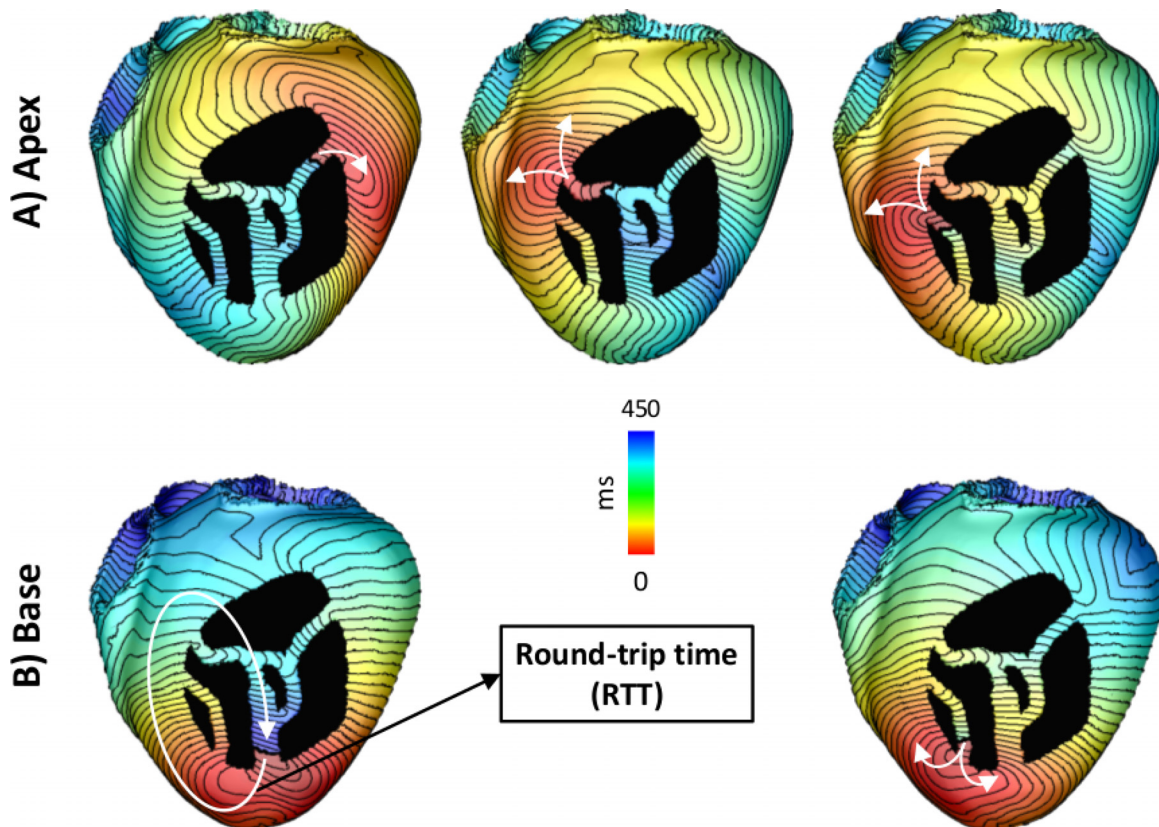


Fig. 6. Pacing locations and induced VTs in the idealized model. VTs associated with exit sites detected after pacing the model at the A) apex (upper panel) and B) base (lower panel). The round-trip time is the time the wavefront takes to travel back to the region of block.

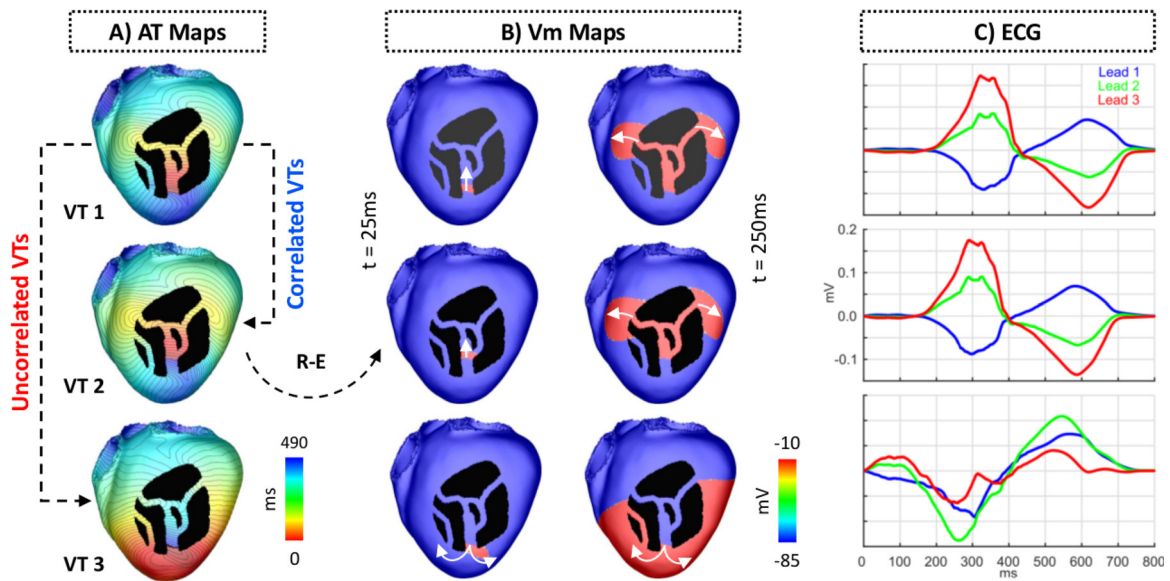


Fig. 7. VT and ECG simulation using the R-E model. A: AT maps of three VTs induced in the idealized model. VT 1 and VT 2 are correlated as they share the same circuit and have the same chirality. VT 1 and VT 3 are not correlated because they have opposite chirality despite sharing the same circuit. B: Snapshots of the transmembrane potential V_m generated by the R-E model at times $t = 25$ ms (left column) and $t = 250$ ms (right column). White arrows represent the direction of propagation. C: ECGs associated with each VT in A. Shown are traces from leads 1, 2 and 3 of the Einthoven's triangle.

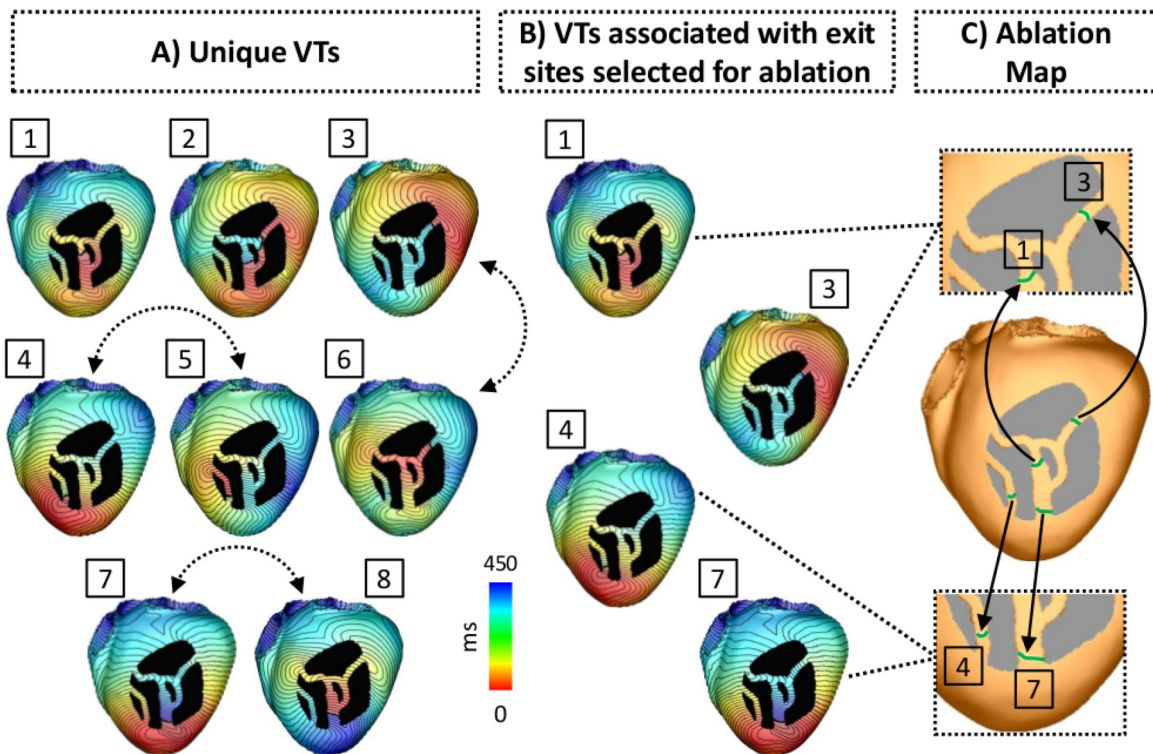


Fig. 8. Unique VTs and ablation targeting in the idealized model. A: Unique VTs detected by VITA after pacing the bi-ventricular model from all 17 locations shown in Fig. 1B. In total, 8 unique VTs were detected. Dashed arrows represent VTs induced from similar exit sites, but have opposite directions. B: VTs associated with exit sites selected for ablation. Among all unique VTs, those associated with exit sites 1, 3, 4 and 7 were optimally selected for ablation. C: Optimal ablation map output by VITA. Ablation lesions are shown in green. Insets show the zoomed-in split surfaces associated with exit sites marked for ablation.

Sections 2.4.1–2.4.2 and the associated VT is triggered by initiating propagation at the proximal face of the block. The choice of sorting the list of exit sites in a descending order of the RTTs is because those are associated with circuits more likely to sustain clinically-relevant VTs. From clinical mapping, sustained VT is more common in circuits with longer isthmuses, whereas non-sustained VT tends

to occur when isthmus dimensions are reduced (Ciaccio et al., 2021). If wavefront arrival is detected at the opposite face of the temporal block, the exit site is virtually ablated, i.e. the block is made permanent. The procedure is repeated for each exit site in the ordered list. The resulting list of selected exit sites form the optimal ablation map shown in Fig. 8C.

The Pseudocode 1 summarizes all steps comprising the VITA algorithm.

2.5. Comparison to current approaches

Following (Arevalo et al., 2013; Ashikaga et al., 2013; Arevalo et al., 2016; Pashakhanloo et al., 2018; Prakosa et al., 2018; Deng et al., 2019b; 2019a), biophysically detailed simulations of VT induction were performed to serve as a basis for comparison with the results obtained with VITA. The monodomain equation was used to simulate the electrical activity within high resolution porcine cohort:

$$\nabla \cdot (\sigma_m \nabla V_m) = \beta I_m, \quad (5)$$

$$C_m \frac{\partial V_m}{\partial t} + I_{ion}(V_m, \eta) - I_{stim} = I_m, \quad (6)$$

$$\frac{\partial \eta}{\partial t} = f(V_m, \eta) \quad (7)$$

where V_m is the transmembrane voltage; β is the surface to volume ratio; I_m is the transmembrane current density; C_m is the membrane capacitance per unit area; I_{ion} is the density of the total ionic current flowing through the cell membrane; I_{stim} is the stimulus current density; and σ_m is the harmonic mean conductivity tensor with eigenvalues given as:

$$\sigma_m = \sigma_i^\zeta (\sigma_i^\zeta + \sigma_e^\zeta)^{-1} \sigma_e^\zeta \quad (8)$$

where $\zeta = l | t$ are the eigendirections of the tissue along the cardiac fiber direction ($\zeta = l$) and transverse ($\zeta = t$) to it (Bishop and Plank, 2010).

Equations were solved using CARPentry which is able to match exactly monodomain simulation results as obtained with the legacy CARP simulator (Vigmond et al., 2003; 2008) used in the reference studies (Arevalo et al., 2013; Ashikaga et al., 2013; Arevalo et al., 2016; Pashakhanloo et al., 2018; Prakosa et al., 2018; Deng et al., 2019b; 2019a). Temporal discretization used an implicit-explicit Crank-Nicolson scheme with operator splitting at a time step of 25 μ s (Niederer et al., 2011). Mass lumping was turned on. Detailed numerical settings are reported in the supplement to enable replication of simulation results with openCARP (Plank et al., 2021).

2.5.1. Electrophysiological parameters

Anisotropic conductivity values of $\sigma_m^l = 0.1361$ S/m and $\sigma_m^t = 0.0176$ S/m were assigned to the myocardium based on intra- and extracellular values reported in the literature (Hooks et al., 2007). The TT model (ten Tusscher and Panfilov, 2006) was used to simulate channel gating and ionic concentrations in cardiac cells (represented by η in Eq. 7). The maximum conductances of the rapid (I_{Kr}) and slow (I_{Ks}) delayed rectifier currents were increased by factor of 2.3 to shorten APD. The resulting APD of 201.5 ms (basic cycle length of 500 ms) falls within the values reported in optical recordings in the porcine heart (Kong et al., 2007).

Furthermore, modifications to the TT model were implemented to represent EP remodelling in the infarct BZ (Arevalo et al., 2013; Ashikaga et al., 2013; Arevalo et al., 2016; Pashakhanloo et al., 2018; Prakosa et al., 2018; Deng et al., 2019b; 2019a). Specifically, the maximum conductances of fast sodium current (I_{Na}) and L-type calcium were reduced to 38% and 31% of their control values, respectively. Also, I_{Kr} and slow I_{Ks} were reduced by 70% and 80%, respectively. These changes resulted in longer APD in the BZ when compared to the healthy myocardium.

Isotropic tissue conductivity with values of $\sigma_{mt} = \sigma_{ml} = 0.064$ S/m (Luke and Saffitz, 1991) were assigned to the BZ in order to account for structural remodelling such as fiber disarray

and presence of fibrosis (Mendonca Costa et al., 2018). The scar was represented as being nonconducting (i.e., by imposing no-flux boundary condition at its interface, sealing the intracellular space there).

2.5.2. Pacing protocol

VTs were induced in the high resolution porcine cohort following the Virtual-heart Arrhythmia Risk Predictor (VARP) (Arevalo et al., 2016) and Virtual-heart Arrhythmia Ablation Targeting (VAAT) (Ashikaga et al., 2013; Prakosa et al., 2018) approaches: a clinical S1-S2-S3 electrical stimulation protocol was applied from 17 pacing sites on each pig model as illustrated in Fig. 1B. This virtual multi-site pacing allows the investigation of a wide range of possible VT morphologies that could arise from a given infarct morphology. For simplicity we will now only refer to this approach as VARP.

Prior to organ-scale pacing, the LV models were initialized with single-cell model states obtained after pacing the TT model for 100 cycles with a basic cycle length of 600 ms. In each LV model, 8 stimuli (S1) at a cycle length of 600 ms were delivered, followed by a premature stimulus (S2) delivered 250 ms after the last S1 beat. The coupling interval of 250 ms was chosen as it was the shortest interval allowing capture in tissue. If the S2 beat did not result in reentry, an additional S3 stimulus was delivered 180 ms (shortest interval required for capture) after the S2 (Arevalo et al., 2016; Pashakhanloo et al., 2018; Prakosa et al., 2018). In all simulations, the virtual pacing electrode had a shape of a half sphere with center at each of the 17 segments in Fig. 1B and 1 mm radius. Stimulation was performed by injecting a transmembrane current I_{stim} as in Eq. 6. Simulations were monitored for 2 s after the last paced beat to detect the presence of VTs. Similar to previous studies (Arevalo et al., 2016; Pashakhanloo et al., 2018), VTs lasting until the end of the 2 s-window were considered sustained. Detection of unique VTs obtained with the VARP approach was performed by visual inspection of wavefronts.

2.6. Simulation of ablation lesions

In-silico ablation was performed according to the ablation maps output by VITA (see Fig. 8). The maps were interpolated from the down-sampled to the high resolution models using Mesh-tool (Neic et al., 2020). The ablation maps represent a very small (optimal) set of targets, which do not aim to replicate clinical lesion dimensions as in previous studies (Prakosa et al., 2018). Ablation lesions were modelled by rendering the tissue (FE elements) at the target areas nonconducting as the necrotic scar. Both VITA and VARP induction protocols as described above were then repeated to assess whether VT could still be induced.

3. Results

The VITA approach presented in the previous sections was tested in the virtual cohort of porcine LV models. The number of arrhythmias induced with VITA was compared to those generated after applying the VARP protocol to the high resolution LV models. Next, a sensitivity analysis was done on VITA. Finally, ablation maps were constructed based on the detected unique VTs.

3.1. VT Inducibility

Table 1 summarizes the number of VTs detected after applying both VITA and VARP approaches to each porcine LV model. Using VITA, VTs were inducible in Pigs 3, 5, 6 and 7. Although numerous VTs were induced in the same model, a subset of these VTs were similar as the same exit site was detected from different pacing locations (see Fig. 7A for details). In Pig 3, for instance, 46 VTs were

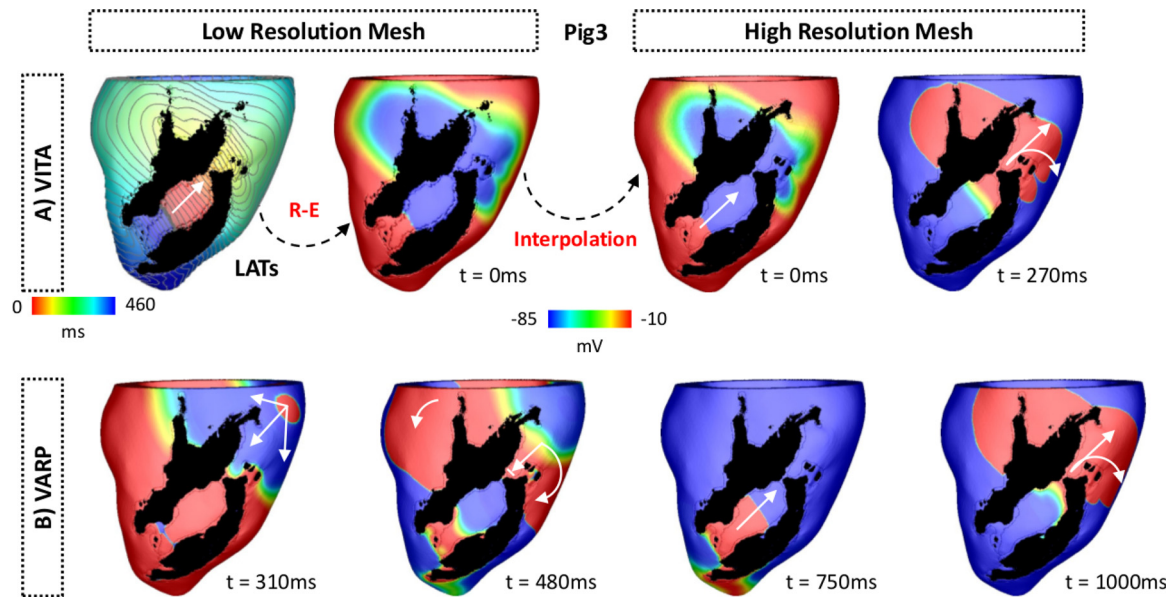


Fig. 9. VT initiation in Pig 3 ventricular model. A: Induced VT using VITA. Top left panel: AT map used to induce VT with the R-E solver within the down-sampled LV model. Top right panel: V_m map interpolated from the low to the high resolution model. V_m map obtained with the R-D model at $t = 270$ ms is also shown. Propagation occurs unidirectionally from the exit site towards the base of the LV. The wavefront travels around the scar and reenters the isthmus from the apex. B: Induced VT using VARP. V_m maps at different times show VT induction following the S1-S2 pacing protocol. White arrows represent successful propagation and lined arrows represent conduction block. The S2 beat was blocked at the isthmus's mouth proximal to the stimulus site ($t = 480$ ms) and, similar to the VT in A, the wavefront revolves around the scar reentering the isthmus ($t = 750$ ms). VT induction in the LV model with both VITA and VARP can be fully appreciated in Supplemental Videos 1 and 2, respectively.

Table 1

Number of VTs induced within the virtual porcine cohort.

| Pig | Induced VTs | | Unique VTs | |
|-----|-------------|------|------------|------|
| | VITA | VARP | VITA | VARP |
| 1 | 0 | 0 | 0 | 0 |
| 2 | 0 | 0 | 0 | 0 |
| 3 | 46 | 15 | 7 | 1 |
| 4 | 0 | 1 | 0 | 1 |
| 5 | 5 | 0 | 1 | 0 |
| 6 | 97 | 12 | 5 | 4 |
| 7 | 75 | 7 | 6 | 3 |

induced, however, only 7 were unique. Overall, more unique VTs were induced with VITA than with VARP. For instance, 7 unique VTs were induced in Pig 3 with VITA while only one was induced using VARP (see Table 1). A fundamental difference in inducibility between VITA and VARP was witnessed in pigs 4 and 5 where only either VITA or VARP induced a VT, but not both.

3.2. Similarity in induced VTs

All VTs associated with an anatomical path detected by VARP were matched up by VITA. In Pig 6, for instance, VITA detected all unique 4 VTs unmasked by VARP plus 1 extra (see Table 1).

Fig. 9 shows VTs induced in Pig 3 using VITA (top panel) and VARP (bottom panel). In VITA, the AT map of the detected VT was fed into the R-E solver and simulated for one cycle (see Section 2.4.4 for details). Both AT and V_m maps show the wavefront propagating in the apico-basal direction. All state variables were then interpolated onto the high resolution mesh in Fig. 9A, top right panel. After leaving the isthmus the wavefront travels around the scar towards the apex ($t = 270$ ms) where it can reenter, forming the circuit sustaining the VT. The VT induced with VITA within Pig 3 can be fully appreciated in Supplemental Video 1.

In VARP, VT was induced after the S2 beat had initially blocked at the isthmus's mouth proximal to the stimulus site ($t = 480$ ms after the S2). As can be seen in Fig. 9B (bottom panel), the wavefront travels around the scar entering the infarct region from a distal site. The wavefront then propagates back towards the base ($t = 750$ ms) exiting through the isthmus from where it reenters the myocardium ($t = 1000$ ms). See Supplemental Video 2 for further details of the block and reentry within Pig 3.

The similarity between the VTs induced by VITA and VARP can be seen at times $t = 270$ ms in Fig. 9B and $t = 1000$ ms in Fig. 9, respectively. Both VTs share the same isthmus and have the same chirality, but the VT induced with VARP takes longer to stabilize following the block of the S2.

3.3. Differences in induced VTs

While more unique VTs were induced by VITA, inducibility in Pig 4 was only possible with VARP (see Table 1). In contrast to all other induced VTs, the electrical reentry underlying this particular case was anchored around a region of functional block rather than an isthmus.

Fig. 10 shows V_m maps following the S2 beat. The wavefront travels throughout the LV until encountering a line of block at the infarct BZ (see Fig. 9, panel $t = 420$ ms). As the BZ tissue distal to the S2 stimulus location recovers excitability, the wavefront can reenter there at $t = 620$ ms. At time $t = 710$ ms the wavefront exits the BZ and propagates to the LV. Note that the reentry sustaining this VT ($620 \text{ ms} \leq t \leq 1000 \text{ ms}$) is anchored in the BZ, where CV is slow due to the reduced tissue conductivity in this region. The conduction block and the evolution of this reentry can be further appreciated in Supplemental Video 3.

Conversely, VT was only inducible in Pig 5 with VITA (see Table 1). This VT revolves around a short circuit with a RTT of 78 ms (data not shown).

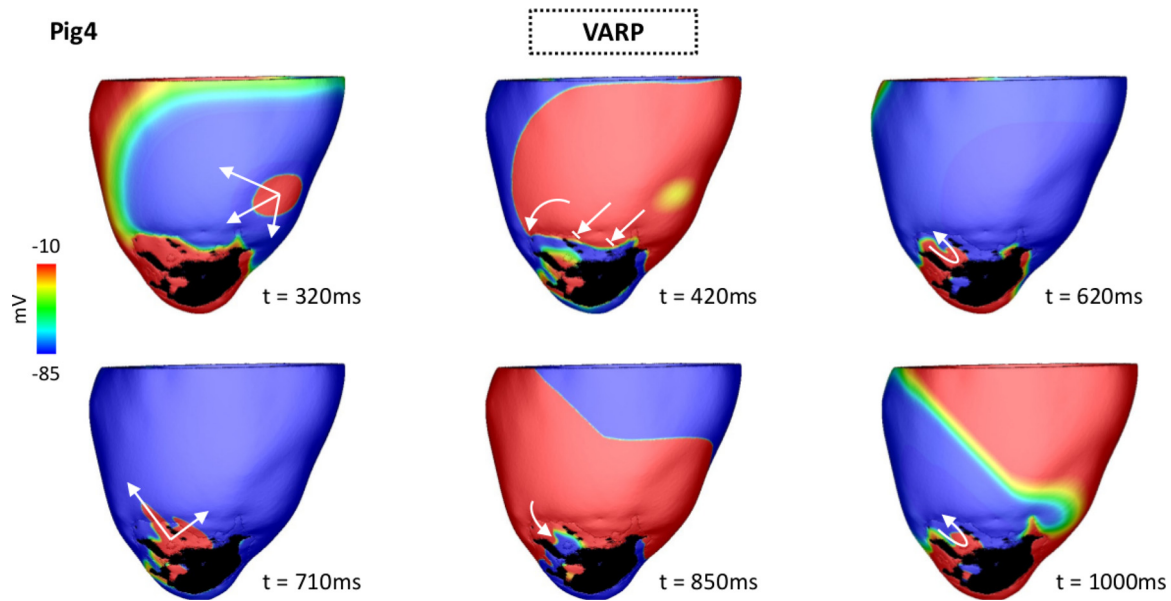


Fig. 10. VT initiation due to functional conduction block in Fig 4 heart model using VARP. V_m maps at different times show VT induction following the S1-S2 pacing protocol. Arrows represent successful propagation. Lined arrows represent conduction block. The S2 beat blocked at the BZ at $t = 420$ ms traveling around the line of conduction block until it reached tissue that had recovered excitability ($t = 620$ ms). At time $t = 710$ ms the wavefront leaves the BZ and enters the LV myocardium. It propagates throughout the LV and returns to the BZ forming a reentrant circuit around the region of functional block. VT induction in the LV model can be fully appreciated in Supplemental Video 3.

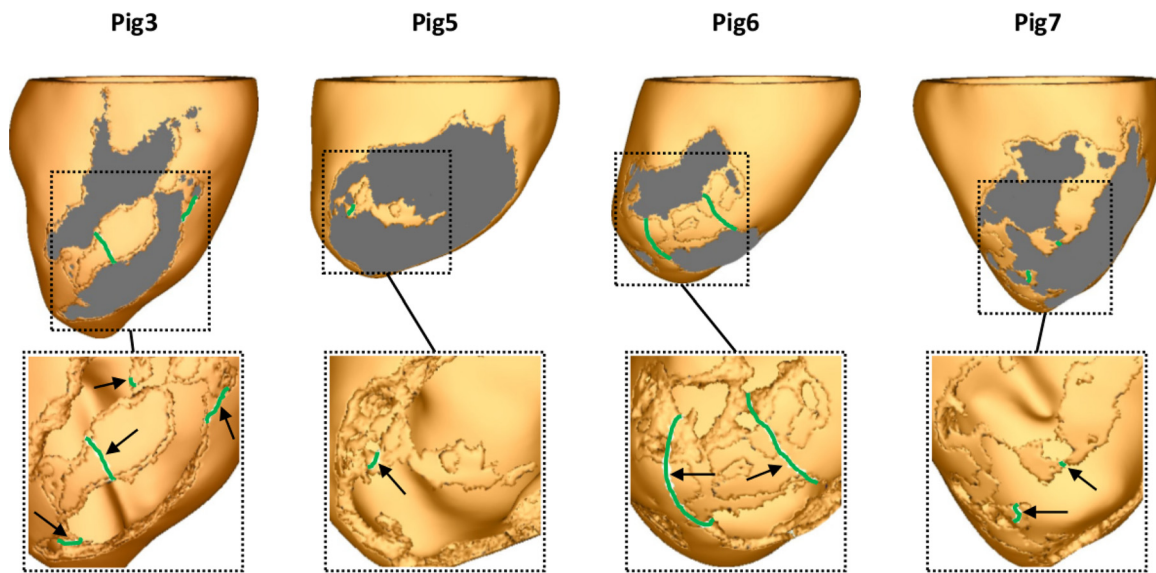


Fig. 11. Optimal ablation targets computed by VITA on the ventricular surfaces of Figs 3, 5, 6 and 7. Ablation lesions are shown in green. Although ablation targets are displayed on LV epicardial surfaces, each lesion represents a transmural 3D isosurface associated with one exit site selected according to the algorithm in Section 2.4.7. Insets show the zoomed-in ablation targets where the scar was removed for visualization purposes. Note the presence of ablation lesions under the scar of Figs 3 and 6.

3.4. Ablation targeting

Once all unique VTs were detected, VITA was employed to detect optimal ablation targets in the virtual hearts. Computed ablation maps in the LV models in which VT was inducible are shown in Fig. 11. Note that in Fig 3 one region selected for ablation is located inside the isthmus rather than at one of its mouths. This is a result of a distance field generated by an initiation site located on the ventricles opposite to the location of the scar. This led to a collision inside the isthmus which was interpreted, according to the definition given in Section 2.4.2, as an exit site by VITA. Size and shape of the ablation targets can be better appreciated in the insets (the scars were removed for visualization purposes). Note the presence of two extra targets located under the scar in Figs 3.

Although ablation targets are displayed on the epicardial surface, they are associated with transmural 3D isosurfaces.

Next, *in-silico* ablation was performed to both low and high resolution models of Fig 3 according to the targets in Fig. 11. To assess the success of the virtual ablation, both VITA and VARP inducibility protocols were repeated in low- and high resolution ablated models, respectively. VTs were no longer inducible in the ablated Fig model.

3.5. Computational performance

The computational costs of both approaches applied to Fig 3 are presented in Tables 2–3. Execution times associated with single as

Table 2
Execution times using VITA on down-sampled models.

| Pacing sites | Module | Desktop time | CPU time |
|--------------|-------------|-----------------|-----------------|
| 1 | VT inducing | 0 h:02 min:49 s | 0 h:47 min:48 s |
| | Ablation | 0 h:00 min:09 s | |
| | ECCG | 0 h:01 min:01 s | |
| | Total | 0 h:03 min:59 s | |
| 17 | VT inducing | 0 h:44 min:34 s | 9 h:35 min:00 s |
| | Ablation | 0 h:01 min:14 s | |
| | ECCG | 0 h:02 min:07 s | |
| | Total | 0 h:47 min:55 s | |

Table 3
Execution times using VARP on high resolution models.

| Pacing sites | HPC time | CPU time |
|--------------|------------------|----------------------|
| 1 | 04 h:02 min:02 s | 1 032 h:40 min:32 s |
| 17 | 68 h:34 min:32 s | 17 555 h:20 min:32 s |

Table 4
Sensitivity analysis of VITA in respect of changes to distance between isosurfaces (D_{iso}). Numbers in parenthesis represent changes in relation to the results obtained with VITA in Table 1.

| Pig | Induced VTs | | Unique VTs | |
|-----|-------------|----------|------------|--------|
| | 0.5 mm | 5.0 mm | 0.5 mm | 5.0 mm |
| 1 | 0 (0) | 0 (0) | 0 (0) | 0 (0) |
| 2 | 0 (0) | 0 (0) | 0 (0) | 0 (0) |
| 3 | 75 (+29) | 33 (-13) | 5 (-2) | 5 (-2) |
| 4 | 0 (0) | 0 (0) | 0 (0) | 0 (0) |
| 5 | 9 (+4) | 2 (-3) | 1 (0) | 1 (0) |
| 6 | 166 (+69) | 59 (-38) | 6 (+1) | 8 (+3) |
| 7 | 98 (+23) | 48 (-27) | 6 (0) | 5 (-1) |

well as multi-site pacing are shown. Execution times refer to the amount of time required by VITA on a 12-core desktop machine and by VARP on 4 nodes (256 cores) of the HPC used in this study (see Section 2.3 for details). CPU time is given by the execution time divided by the total number of cores used in the simulations. When pacing from only one location, VITA could induce VTs, detect ablation targets and simulate ECCGs in 4 min on a desktop, while VARP required 4 h of simulation time on a HPC machine. Multi-site pacing increased execution times to about 48 min and 68 h:34 min using VITA and VARP, respectively. Considering CPU time, VITA was, on average, 1 564 times faster than VARP.

3.6. Sensitivity analysis

Sensitivity analysis was done to key parameters of VITA: distance between isosurfaces (D_{iso}), RTT and the anisotropic CVs used as parameters for the Eikonal model (Eq. 2).

3.6.1. changes in D_{iso}

Table 4 shows the number of VTs detected by VITA when D_{iso} is decreased from 1.0 mm (default value) to 0.5 mm and increased to 5.0 mm. As in Table 1, VTs were induced in Pigs 3, 5, 6 and 7. The change in number of VTs was inversely related to changes in D_{iso} . The number of unique VTs did not follow this trend, decreasing in Pig 3 while increasing in Pig 6.

The effects of changes in D_{iso} on ablation targets computed within Pig 3 are summarized in Fig. 12. Although changes in D_{iso} affected the number of unique VTs, the ablation targets remained similar (compare panels Fig. 12 in B) for constant RTT = 50 ms). However, two VTs associated with the presence of a small isthmus near the apex were not detected when D_{iso} was decreased to 0.5 mm. As a result, the more apical ablation target seen on maps computed with $D_{iso} = 1.0$ mm and $D_{iso} = 5.0$ mm is not seen for

Algorithm 1 VITA.

Require: \mathcal{L} : set of pacing locations, \mathcal{M} : mesh, ϵ : maximum surface fragment size, γ : round-trip-time threshold

- 1: $\mathcal{V} \leftarrow \{\}$ ▷ set of unique VTs
- 2: **for** $l \in \mathcal{L}$ **do**
- 3: $d(x) \leftarrow \text{dist}(\mathcal{M}, l)$ ▷ compute distance field
- 4: $\{s_i\} = \mathcal{S} \leftarrow \text{isosurf}(\mathcal{M}, d)$ ▷ compute isosurf fragments
- 5: $\mathcal{S} \leftarrow \mathcal{S} \setminus \{s_i \mid \|s_i\| > \epsilon\}$ ▷ discard fragments outside of isthmus
- 6: $\mathcal{S} \leftarrow \mathcal{S} \setminus \{s_i \mid s_i \text{ has downstream neighbours}\}$ ▷ keep only exit sites
- 7: **for** $s_i \in \mathcal{S}$ **do**
- 8: $\mathcal{M}^* \leftarrow \text{split}(\mathcal{M}, s_i)$ ▷ decouple connectivity of \mathcal{M} at interface s_i
- 9: $v(x) \leftarrow \text{eikonal}(\mathcal{M}^*, s_i)$ ▷ Eikonal solution starting at one side of s_i
- 10: $r \leftarrow \min_{x \in s_i} (\text{rtt}(v))$ ▷ minimum round-trip-time at interface s_i
- 11: **if** $r \geq \gamma$ **then**
- 12: $\mathcal{V} \leftarrow \mathcal{V} \cup \{v\}$
- 13: **end if**
- 14: **end for**
- 15: **end for**
- 16: $\mathcal{V} \leftarrow \mathcal{V} \setminus \{v \mid v \text{ not unique}\}$
- 17: $\mathcal{G} \leftarrow \text{egm}(\mathcal{M}, \mathcal{V})$ ▷ compute electrograms
- 18: $\mathcal{B} \leftarrow \text{ablation}(\mathcal{M}, \mathcal{V})$ ▷ compute ablation targets
- 19: **return** $\mathcal{V}, \mathcal{G}, \mathcal{B}$

Table 5
Sensitivity analysis of VITA in respect of changes to RTT from 50 ms to 200 ms. Numbers in parenthesis represent changes in relation to the results obtained with VITA in Table 1.

| Pig | Induced VTs | Unique VTs |
|-----|-------------|------------|
| 1 | 0 (0) | 0 (0) |
| 2 | 0 (0) | 0 (0) |
| 3 | 23 (-23) | 2 (-5) |
| 4 | 0 (0) | 0 (0) |
| 5 | 0 (-5) | 0 (-1) |
| 6 | 25 (-72) | 6 (+1) |
| 7 | 26 (-49) | 2 (-4) |

case of $D_{iso} = 0.5$ mm. The major effect of changes in D_{iso} was observed in execution times. Decreasing D_{iso} from 1.0 mm to 0.5 mm led to a 2-fold increase in the time to perform the VT inducing module in VITA: from 44 min:34 s (Table 2) to 01 h:29 min:20 s. Increasing D_{iso} to 5.0 mm shortened the VT detection time to 10 min:58 s.

3.6.2. Changes in RTT

Effects of increasing RTT from 50 ms to 200 ms are presented in Table 5. Overall, a longer RTT led to fewer detected VTs. Note that increasing RTT resulted in no VT being detected in Pig 4. As shown in Fig. 12, a longer RTT reduced the number of unique VTs detected by VITA as these are associated with smaller reentrant pathways. Execution times were not affected by RTT.

The effects of a longer RTT on unique VTs and ablation targets computed within Pig 3 can be seen in Fig. 12. Note that the location of the unidirectional block inside the isthmus shifted by changing RTT.

3.6.3. Changes in CV

Finally, CVs in the longitudinal and transverse fiber directions in both healthy myocardium and BZ were modified to $\pm 25\%$ of their

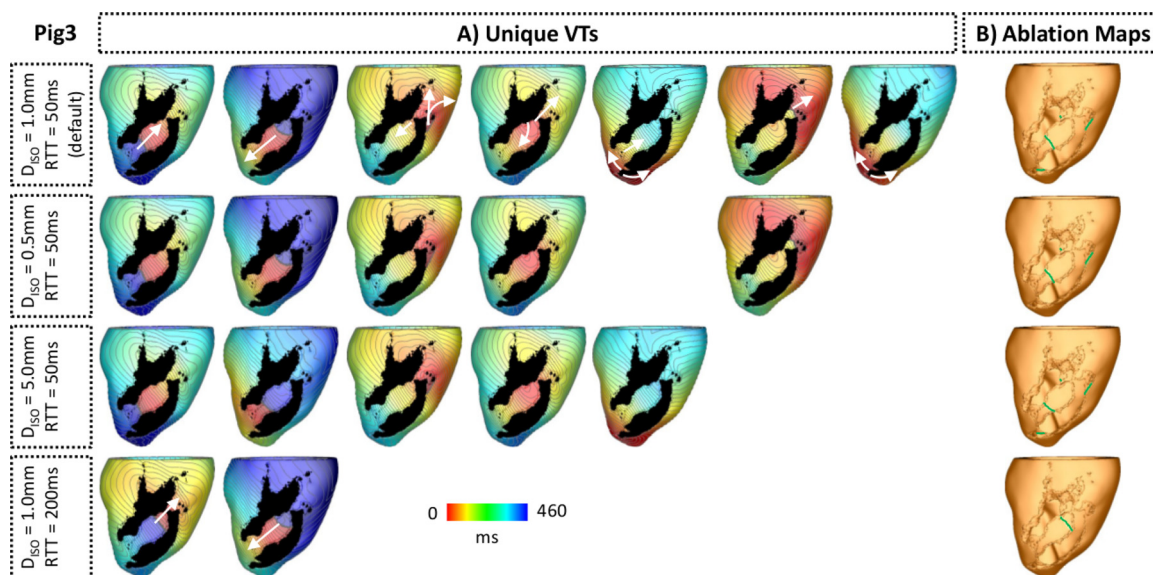


Fig. 12. Effects of D_{iso} and RTT on number of unique VTs and ablation targets in Fig 3. A: Unique VTs detected by VITA after applying the multi-site pacing in Fig 3 for each value of D_{iso} and RTT under investigation. B: Optimal ablation maps generated by VITA based on exit sites associated with the unique VTs in A. The scar was removed to allow visualization of lesions located in the endocardium.

Table 6

Sensitivity analysis of VITA in respect of changes to CV. Numbers in parenthesis represent changes in relation to the results obtained with VITA in Table 1.

| Fig | Induced VTs | | Unique VTs | |
|-----|--------------------|--------------------|--------------------|--------------------|
| | CV _{-25%} | CV _{+25%} | CV _{-25%} | CV _{+25%} |
| 1 | 0 (0) | 0 (0) | 0 (0) | 0 (0) |
| 2 | 0 (0) | 0 (0) | 0 (0) | 0 (0) |
| 3 | 46 (0) | 46 (0) | 6 (-1) | 7 (0) |
| 4 | 0 (0) | 0 (0) | 0 (0) | 0 (0) |
| 5 | 5 (0) | 0 (0) | 1 (0) | 0 (-1) |
| 6 | 92 (-5) | 97 (0) | 7 (+2) | 5 (0) |
| 7 | 81 (+6) | 75 (0) | 6 (0) | 6 (0) |

default values. The results of the sensitivity analysis are summarized in Table 6. Changes in CV had a slight effect on the number of VTs. The largest change in induced VTs was observed in Fig 7, where the number of VTs increased from 75 (Table 1) to 81 for CV_{-25%}, but remained the same for CV_{+25%}. However, this increase was not reflected in the number of unique VTs which remained the same as in the control case. Altogether, the number of unique VTs was marginally changed by increasing or decreasing CV in all hearts.

4. Discussion

We presented a novel, rapid and fully automated computational approach which can be applied to post-infarcted heart models for the purpose of: 1) locating reentrant circuits maintaining scar-related VTs; 2) simulating AT maps and ECGs of such VTs; and 3) computing targets to guide ablation therapy in near real-time. Using only standard desktop computational resources, VITA was shown to be capable of detecting and simulating AT maps of VTs as well as automatically, without operator intervention, generating an optimal ablation map in 48 min. Our approach also facilitates the fast simulation of EGMs and ECGs of each uncovered VT circuit, offering the opportunity to compare the simulated ECG or EGM signatures to those recorded clinical, either prior to or during catheter

ablation therapy and, thus, confirm the electrophysiological correspondence between simulated and clinical VT.

4.1. Comparison with R-D approaches

In-silico VT induction protocols have proved to be a highly useful and robust way to reliably induce (multiple) complex arrhythmias in the context of structural heart disease. Such methods have been successfully applied to demonstrate the potential utility of an *in-silico* approach in guiding VT ablation planning (Prakosa et al., 2018) and also arrhythmic risk stratification (Arevalo et al., 2016). The majority of VT inducibility studies, particularly for direct use in a clinical workflow (Arevalo et al., 2016; Prakosa et al., 2018), have been based on sophisticated R-D models. The advantage of R-D is that these models accurately replicate cardiac electrophysiology, including the mechanisms underlying formation and maintenance of arrhythmias, usually through a monodomain representation of tissue-level electrophysiology, along with biophysically-detailed ionic cell models representing sub-cellular dynamics. Consequently, in the context of personalized clinical modelling, R-D approaches may be considered to constitute a more physiologically-accurate representation of a patient’s heart to probe VT inducibility. R-D based VT induction protocols have also been widely used by ourselves (Campos et al., 2019; Monaci et al., 2021) (in more abbreviated forms) and others (Deng et al., 2015; Pashakhanloo et al., 2018; Lopez-Perez et al., 2019; Deng et al., 2019a) in more basic mechanistic studies, investigating the properties of arrhythmias and consequential modelling considerations in this regard.

However, R-D approaches suffer from two main disadvantages. Firstly, the compute costs required to conduct such a large number of expensive monodomain simulations are punitive, rendering inducibility testing a costly endeavor; the subsequent requirement for off-site HPC facilities hampers the use of such approach within a real clinical workflow. In comparison, VITA required only a fraction of the computational time of the corresponding R-D approach (VARP) to achieve the same goal of uncovering scar-related VTs in infarcted ventricular models. Specifically, more than 68 h:30 min of computing time was required to implement the full VARP protocol on an HPC cluster (256 CPUs). Using only a fast desktop machine (with 12 CPUs), VITA brought this time down to approxi-

mately 48 min which is compatible for use within a clinical procedure.

There are other ways to make VARP faster than the specific implementation we refer to. However there are trade-offs to keep in mind, in particular meshes with coarse resolutions can produce numerical artifacts. Numerical as well as computational techniques that enable the rapid solution of the equations underlying VARP on highly detailed cardiac electrophysiology models have been a topic of research in our group and others (dos Santos et al., 2004; Plank et al., 2007; Niederer et al., 2011). Graphics processing units (GPUs) offer a promising alternative to simulate the electrical activity in the heart due to their highly parallel processors with tremendous computational horsepower and high memory bandwidth (Rocha et al., 2011; Neic et al., 2012; Campos et al., 2016; Lim et al., 2020; Vasconcellos et al., 2020). The use of monolayer meshes is also an alternative to speed up biophysically-accurate simulations as demonstrated by Lim et al. (Lim et al., 2020) in an *in-silico* atrial model. However, the transmural anatomy of the scar and fiber orientation within the ventricles require 3D meshes. Another form to decrease the computational overhead associated with R-D simulations is to use simpler ionic models within low resolution meshes. However, an under-resolved mesh would mean that functional block (which is very sensitive to mesh resolution) would happen too often along with poor representation of conduction slowing and at head-tail collisions (Kléber and Rudy, 2004; Coronel et al., 2009). Here, we propose a faster method that is based on solving a topological problem yet still incorporates the important high-resolution structural information of the 3D ventricular geometry and infarct anatomy. VITA extracts all viable anatomical circuits present in the model regardless of mesh resolution.

Secondly, R-D models intrinsically use high-dimensional parameter vectors. Such parameters, principally for the ionic cell models, primarily govern tissue excitability and refractoriness, and thus directly influence arrhythmia induction (through unidirectional block) and maintenance (through electrical wavelength). If these values were altered (*i.e.*, longer APDs or altered CVs), functional block may not occur, or may occur in other areas. The vast majority of these parameters used cannot be constrained to this level of detail with currently available clinical data. Consequently, VT inducibility using R-D approaches has a strong functional component, which is not patient-specific, but instead relies on literature values for parametrization. In comparison, VITA only detects vulnerable sites associated with the anatomical presence of an isthmus within a non-conducting scar. The only functional parameter in VITA relates to the RTT (or, equivalently the assigned CV), which may be more easily tuned to match the known VT cycle length, and even directly compared through EGM/ECG simulation with the clinical VT. This important aspect of comparison and validation in clinical *in-silico* VT simulation studies with personalized models has so far been lacking (Prakosa et al., 2018).

In the context of scar-related VT, anatomical isthmuses (with non-conducting scar on both sides (Ciaccio et al., 2021)) represent the most common substrate. This is underscored by the recent suggested success of directly using “de-channeling” analysis of CMR data to directly locate isthmuses and guide ablation procedures (Sánchez-Somonte et al., 2021; Berrueto et al., 2015). Consequently, both approaches, VITA and the R-D based VARP, show very similar performance at uncovering unique VTs in each LV model in the virtual cohort (Table 1). In fact, all VTs associated with an anatomical path detected by VARP were matched up by VITA.

Nonetheless, functional block may form an important substrate to sustain VT which cannot be identified, in its current form, by VITA. Channels formed within a region of functional conduction block, where one entrance to an isthmus continually blocks the reentrant wave as it is refractory at the time of the wave’s passage, with the other side formed by non-conducting scar (Deng et al.,

2019b), such as the one in Fig. 10, could only be detected in full-blown R-D simulations, as used with VARP. However, the appearance of such regions of functional block depends sensitively on the specific electrophysiological properties assigned to the healthy tissue and BZ within the model, which thus control the relative degree of refractoriness between these regions. Currently, in the VARP approach, electrophysiology is not personalized in any way, relying purely on generic literature values of ionic conductances and tissue conductivities. Whether these regions of functional block are really present in this particular patient/model is unknown, and thus their identification may be of limited value in a clinical context of a personalized therapy.

4.2. Comparison with R-E approaches

Alternatively, VT inducibility has also been presented in personalized models using Eikonal approaches (Relan et al., 2011; Chen et al., 2016; Cedilnik et al., 2018). Such studies, like VITA, benefit from a more computationally efficient methodology, requiring less than 1 min to simulate a full VT activation map (Cedilnik et al., 2018); this is similar to the time required by the VT inducibility module of VITA, which runs Eikonal simulations for each exit site detected from a given pacing time (Table 2). However, these studies have not explicitly tested for inducibility, as induction was enforced by a local unidirectional block whose location (and direction) required prior interactive manual identification. Subsequent simulation of AT maps of the ensuing VT was compared to electroanatomical mapping data, but was not used for identifying the substrate. Ablation targeting relied entirely on image analysis, and was not guided by the *in-silico* simulation. In VITA, the detection of vulnerable regions (distal mouths, *i.e.*, exit sites of isthmuses capable of sustaining VTs) and the respective unidirectional block simulation is done in a fully automated way.

The dynamics of VT circuits detected on down-sampled meshes using the R-E model can also be directly investigated in matching high resolution R-D models. This is achieved by projecting the electrophysiological tissue state during a VT from a lower resolution onto a high resolution grid using Meshtool (Neic et al., 2020), and by adjusting conductivities for the high resolution grid to match conduction velocities (Costa et al., 2013). Unlike simulations within the low resolution meshes, tissue conductivities in high resolution models, such as the one in Fig. 9A, may not need to be altered to match prescribed velocities. However, R-D simulations within high resolution models come with a higher computational cost (see Table 3).

4.3. Automated ablation target identification

In this study, VTs were induced using a similar pacing protocol to VARP studies (Arevalo et al., 2016; Prakosa et al., 2018). However, ablation maps were only automatically computed when using VITA as the minimum cut algorithm used in VARP studies was not available to us (Zahid et al., 2016; Prakosa et al., 2018). Many of the ablation targets detected by VITA might not be necessary for preventing inducibility using VARP as these reflect small reentrant circuits of non-sustained VTs that terminate in R-D simulations due to head-tail collisions (Kléber and Rudy, 2004; Coronel et al., 2009). However, a VITA-based ablation according to activation maps generated with VARP would require an isosurface list of exit sites to be used to disconnect nodes in the mesh. This is not provided by the VARP simulations, only an AT map of the VT circuit. However, to demonstrate the ability of the set of VITA ablation lesions to render virtual hearts VT-free the VARP protocol was applied to Fig 3 model. VITA was also repeated on the ablated model to investigate whether new channels were formed as a result of the ablation. The LV model was ablated according to the

targets identified by VITA (maps in Fig. 11). VT was no longer inducible in the newly ablated model, demonstrating the ability of our approach to eliminate structural substrates sustaining VT.

Exit sites rather than entries were chosen to construct ablation maps here as they serve as an important guide for catheter ablation therapy. However, some of the detected exit sites were not exactly located at one of the isthmus' mouths due to collisions of isosurfaces at those regions (see Fig 3 in Fig. 11 for example). While VITA aims to output a minimal set of ablation lesions, these have the purpose of aiding in clinical decision making. More important are the AT maps of all detected unique VTs detected by VITA. AT maps can highlight the whole VT circuit and provide the information for successful ablation of the reentrant circuit and subsequent VT termination.

The simulated ablation lesions here are rather simplistic compared to the clinical protocol where the operator often titrates the power/energy/time to creating more than one lesion onto a suspected exit site to ensure a complete circuit interruption. In this study, the creation of virtual ablation lesions was purposefully not attempted due to the aforementioned variability in the clinical delivery of the lesion(s) itself, once a target has been identified. VITA aims to identify "targets" which successfully interrupt the anatomical reentrant circuit, specifically highlighting the minimal tissue to be rendered unexcitable to ablate. Thus, ablating or interrupting the circuit at this site will prevent reentry from occurring.

4.4. Parameter sensitivity

Owing to its computational efficiency, VITA is ideally suitable for exploring the sensitivity of its output (unique VTs, corresponding circuits and ablation targets) to key input parameters (both of the VITA algorithm itself and related the electrophysiological properties).

4.4.1. D_{iso}

While the number of VTs changed with D_{iso} (Table 4), the main impact of increasing D_{iso} was the reduction in computational time. A larger D_{iso} results in less split isosurfaces inside the isthmus speeding up the algorithm. The computational cost associated with the VT induction step of VITA in Fig 3 decreased by about a factor of 4 (from 44 min:34 s to 10 min:58 s), as D_{iso} increased from 0.5 mm to 5 mm.

4.4.2. RTT

The VT cycle length is an estimation of the time needed by the wavefront to complete one full cycle around a reentrant pathway. VTs with cycle lengths ranging from 127 ± 72 ms to 365 ms have been reported in the literature (Volosin et al., 1991; Nishimura et al., 2021). This time is taken into account by adjusting RTT in VITA (see Fig. 6). This can be done also in a patient-specific manner, guided by pre-operative recordings of the clinical VT, where available. Moreover, a VT is sustained only if the cardiac wavelength given by $CV \times ERP$ (effective refractory period) is shorter than the physical length of the circuit. VT maintenance is assessed in VITA by ensuring that the RTT of the electrical reentry is above a threshold that can be either tuned to the cycle length of the clinical VT or probed to reveal the existence of smaller circuits. A longer RTT of 200 ms resulted in less VTs being detected as reentrant circuits associated with shorter path lengths were disregarded by the algorithm (see Table 5). Indeed, the shorter circuit associated with the only unique VT detected in Fig 5 was ignored when RTT was prolonged to 200 ms. Interestingly, the use of a longer RTT resulted in a similar number of unique VTs by VITA (Table 5) and VARP (Table 1). This is likely due to the longer APD in the BZ that prevented reentry of wavefronts at isthmuses associated with shorter circuits (Campos et al., 2019).

The change in the number of unique VTs when altering RTT also affected the predicted ablation map as shown in Fig. 12. RTT may vary from patient to patient as well as during the ablation procedure. By considering a very short RTTs (50 ms), VITA was capable of unmasking all possible circuits, even those with RTT smaller than typical VT cycle lengths. Such small circuits might not be able to sustain clinically relevant VTs at a specific stage of the disease. However, remodelling process that progressively slow CV or shorten APD within the isthmus could reduce the wavelength, allowing these channels, potentially, to sustain VTs (Mendonca Costa et al., 2018). Thus, by detecting isthmuses associated with a short RTT, VITA may potentially eliminate the need for repeated ablations due to VT recurrence.

4.4.3. EP Properties

Most *in-silico* studies use patient-specific geometry, but patient-specific EP in both healthy tissue and BZ have been absent as such invasive data is often not available. However, one of the main advantages of VITA is that while known local variation in EP data (*i.e.*, CV in the isthmus) may be difficult to personalize, this is not crucial. Global or local (*e.g.* infarct BZ) CVs may be tuned to obtain RTTs that reflect the VT cycle length from a device, or personalized from patient QRS durations. The computational efficiency of VITA allows for a thorough sweep over distribution of CVs, including variation around the scar that could uncover VT circuits that may form only for short wavelengths. The resulting RTTs can then be used for assessment of consistent ablation targets. We found that inducibility in all models was similar despite the relatively large changes in CV applied ($\pm 25\%$) simultaneously to both healthy myocardium and BZ. Overall, changes to CV had the expected effect on VT inducibility: decreasing CV shortened the wavelength of the AP, allowing to fit an entire AP inside smaller reentrant circuit (more unique VTs). The increase in CV had the opposite effect, leading to fewer VTs induced as shorter circuits were not able any more to fit an entire AP wave with a minimum excitable gap. These findings are in accordance with a previous study using full-blown R-D simulations, which demonstrated that VT localization is fairly insensitive to EP variability, suggesting that infarct anatomy plays the major role in formation and maintenance of scar-related VTs (Deng et al., 2019b).

4.5. Utility in clinical applications

VITA automatically identified exit sites defined here as distal mouths of channel isthmuses within the scar. Exits rather than entries were chosen here because they identify the point of activation of the myocardium and therefore serve as an important guide for catheter ablation therapy. We have shown that our novel approach can faithfully reproduce VT circuits within infarcted models, similar to previously used approaches relying on R-D models (VARP). For these their clinical utility in stratifying arrhythmic risk or in guiding catheter ablation targets has been demonstrated already with real patient models (Arevalo et al., 2016; Prakosa et al., 2018). However, the computational costs of VARP-like approaches relying on the availability of HPC resources is almost prohibitively expensive for clinical applications. An important advance of our method in this regard is the ability to yield comparable results at a fraction of the costs. VITA is orders of magnitudes more efficient and can be executed with standard desktop computing power. The efficiency of VITA opens up perspectives of optimizing VT ablation, either off line pre-operatively or, potentially, online during the ablation procedure itself.

A major issue in VT ablation is identifying the clinical VT responsible for the patient's presentation. To trust computational models to be used in therapy optimization evidence is needed to demonstrate that modelled VT circuits correspond closely to the

clinical VT observed in a given patient. VITA as implemented in here based on a R-E model offers detailed electrophysiology simulations with close to real-time performance (Gillette et al., 2021), allowing to produce all data relevant for comparing with EAM systems, including device and catheter EGMs as well as ECGs or body surface potential maps. ECGs and EGMs in our study were computed based on the ϕ_e -recovery method that relies on simplifying assumptions (Plonsey and Barr, 1998). This could be replaced with the computationally more efficient lead field method, that yields EGMs of maximum biophysical fidelity (Potse, 2018; Gillette et al., 2021). This combined approach facilitates the rapid and accurate simulation of EGM recordings associated to VTs as they are measured e.g. by implantable cardioverter defibrillators (ICDs) which the vast majority of ablation patients have *in-situ*, as performed in our own recent study (Monaci et al., 2021). Such an ability provides the potential for direct comparison with pre-operative recordings of the clinical VT from patient ICDs (or, alternatively, ECG measurements, if available), allowing a direct matching of simulated VT circuit (and ablation targets) with the clinical VT of a given patient. Close matching of EGM and ECG wave forms can be considered an important pathways towards enhancing credibility and clinical confidence in simulated predictions.

Due to its speed, VITA can not only be used to directly match the clinical VT cycle length (if known, for example, from ICD recordings) through the RTT parameter, but also used to uncover any potential VT circuit and ablation target by varying this parameter and repeating the analysis. This may not only facilitate the targeting of the clinical VT, but also, potentially, reducing the need for re-do procedures by ensuring that other possible substrates are eliminated at the time of initial ablation.

4.6. Clinical imaging and model construction

It is important to note that the accuracy and overall utility of our method, in a similar manner to all previous works in this field, depends upon the fidelity of the clinical imaging and subsequent segmentation performed to construct the computational model. Different segmentations (due to low resolution scar imaging) will lead to anatomical structures not being accurately represented or completely absent in the geometrical model. In this scenario, VITA (as well as VARP) will inevitably fail to induce VT. Here, we utilized 1 mm isotropic CMR, which is higher resolution than most current clinical acquisitions. Such a resolution is important to robustly identify the structural anatomy of critical isthmuses through the scar which represented the substrate for sustaining the VT. However, previous studies have used clinical CMR acquired at similar in-plane resolution (1-2 mm), but much lower slice spacing of 8-12 mm and, employing the R-D approach, were still able to induce VT and compute optimal ablation targets (Ashikaga et al., 2013; Deng et al., 2015; 2019a; Prakosa et al., 2018), being compared with clinical targets. Here, we focused on directly comparing our novel approach (VITA) with the existing R-D gold standard on the same models from the same resolution imaging. Although no experimental VT ground truth was available for validation, VITA was always capable of uncovering all anatomical reentrant circuits identified by VARP, importantly in addition to "extra" circuits missed by VARP (see Table 1). The absence of certain circuits, due to "missing" isthmuses or blocked-up channels because of lower resolution/inadequate imaging, would also not have been identified by VARP, as these circuits simply would no longer be there.

Further, the impact of different resolution CMR data on infarct morphology representation and subsequent differences in scar-related VT simulation has been investigated recently by our group (Mendonca Costa et al., 2022). The study concluded that high resolution imaging was required to accurately represent scar

morphology in models used to simulate VT. To investigate this specific issue, VITA was further tested on the down-sampled version of Fig 3 used by Costa et al. (Mendonca Costa et al., 2022) and compared the results to VARP. In this coarse-scar model, 6 unique VTs were induced using VITA compared to only one induced by VARP. This result is similar to that reported in Table 1. Furthermore, meshes with average FE edge lengths of slightly higher resolution than those of the CMR scans were used here as mesh resolution does not depend on image resolution. The accuracy of the mesh and consequently the ability of VITA to accurately detect critical isthmuses within the scar depend on the quality of the images (as discussed above).

Nonetheless, imaging capabilities and sequences are continually improving (Orini et al., 2021). With a recent drive towards fully 3D CMR nearly it is anticipated that higher resolution 3D MRI will become standard clinical practice (Milotta et al., 2021). Cardiac CT may also provide a reliable alternative to CMR with a higher sub-millimeter resolution, but currently still requires further development for reliably delineating scar and unnecessary exposure to radiation. The combination of VITA with these current advances in cardiac scar imaging will facilitate full clinical translation of such computational approaches. Thus, issues surrounding adequate image resolutions for model construction may well be obsolete in the foreseeable future. Beyond anatomy, image analysis to delineate scar and BZ from viable healthy myocardium is even more important. Validation and optimization of segmentation approaches are also rapidly evolving for both CMR (Karim et al., 2013; Razeghi et al., 2020) and CT (Yamashita et al., 2016; Cedilnik et al., 2018), which will facilitate, the robust and accurate model generation from higher resolution clinical images.

In addition, the majority of patients undergoing VT ablation therapy have ICDs *in-situ* prior to ablation procedures, which can cause artifacts in CMR images. Such artifacts can be variable, rendering segmentation for an accurate model construction more challenging but still feasible (Prakosa et al., 2018). The evolution of novel wideband sequences is addressing the need for suppressing artifacts in patients with cardiac implanted electronic devices (Rashid et al., 2014; Ranjan et al., 2015; Rashid et al., 2016). Finally, refinements in contrast and dual-energy CT imaging, along with extra-cellular volume reconstructions, also promises potential utility for deriving robust information about scar anatomy for computational infarct model constructions. With CT imaging device artifacts are less prominent and overall image resolution is intrinsically higher relative to CMR.

4.7. Limitations of VITA

As discussed previously, one of the main limitations of VITA is that its outcome relies on the quality of the segmented images. However, this shortcoming will be lessened by the continuous advance in both data acquisition and image analysis to delineate scar and BZ from healthy tissue. Also, in its current form VITA is not suitable for studying functional VTs. Functional conduction block results from dispersion of repolarization. Such detail cannot yet be robustly acquired by current EAM systems, which renders representation of such electrophysiological detail in a patient-specific manner not possible in this approach or any other. Further, while VITA allows for fast simulation of ECGs and EGMs, a comparison between these and the dynamics of the clinical VT in a patient-specific manner has not been performed yet. Such direct comparison may also require patient-specific tuning of CV and RTT in VITA to accurately match the presenting VT. Furthermore, anatomical structure may develop and change during the course of disease progression (structural remodelling - from days to months), emphasizing the requirement of imaging used for model construction just prior to ablation therapy planning for optimal model-

based predictions. Finally, validation is a crucial step to ensure that a computational model can predict the outcome of an experiment. A full “validation” of VITA would require a prospective clinical trial, including long-term patient follow-up post-procedure to: 1) verify that the VT circuits detected by VITA are the same as in the patient, e.g. by demonstrating a match in VT signature in ECG or EGMs between simulation and clinical data; 2) demonstrate that the chosen ablation sites indeed interrupt the VT circuit; and, 3) that the patient is free from VT long-term. An *ex-vivo* study with high density pre- and post-ablation 3D high resolution mapping would be an alternative to a clinical trial. However, it is currently not feasible. Moreover, a validation of induction and treatment (through ablation) of VTs is problematic due to the lack of a clear ground truth. Ultimately, ablation success relies on accurate detection and elimination of reentrant circuits. In this study we propose a novel model capable of detecting the VT exit site, based entirely on topological considerations. Here, we focus on the methodological description of the approach taken by VITA, along with an important comparison with the currently-used traditional R-D methods (VARP). Such methods have themselves been compared (qualitatively) with clinical studies, both in the context of being able to perform virtual VT induction protocols (Arevalo et al., 2016), identify reentrant circuits and subsequently target key ablation sites both in pre-clinical studies (Pashakhanloo et al., 2018; Deng et al., 2019a) and in the clinic (Ashikaga et al., 2013; Prakosa et al., 2018).

5. Conclusion

This study presented a novel automated computational tool for induction and treatment of scar-related VTs in near-real time. VITA was shown to be capable of rapidly detecting VT exit sites, simulating AT maps and ECGs as well as to output an optimal set of targets for catheter ablation therapy. The rapid algorithmic approach proposed here, combined with personalization techniques for building digital twin models that facilitate the detailed replication of electrophysiological recordings, may be used as a complementary modality aiding in clinical decision making in the treatment of post-infarction VTs.

Declaration of Competing Interest

None.

Acknowledgments

This research was supported by the National Institute for Health Research (NIHR) Clinical Research Facility at Guy's and St. Thomas' National Health Service (NHS) Foundation Trust and NIHR Biomedical Research Centre based at Guy's and St. Thomas' NHS Foundation Trust and King's College London. The views expressed are those of the authors and not necessarily those of the NHS, the NIHR or the Department of Health. Open access for this article was funded by King's College London. This research was funded in whole, or in part, by the Wellcome Trust [213342/Z/18/Z]. For the purpose of open access, the author has applied a CC BY public copyright license to any Author Accepted Manuscript version arising from this submission. FOC and MJB acknowledge the support of the British Heart Foundation through Project Grant PG/16/81/32441. AN acknowledges the support of the grant FO999891133 from the Austrian Research Promotion Agency (FFG). JW acknowledges the support of the Wellcome Engineering and Physical Sciences Research Council (EPSRC) Centre for Medical Engineering at King's College London (WT 203148/Z/16/Z), the Health Innovation Challenge Fund (HICF-R10-698), a parallel funding partnership between the Department of Health and the Wel-

come Trust, and the EPSRC grant (EP/R010935/1). MJB acknowledges the support of the UK Medical Research Council through a New Investigator Research Grant number MR/N011007/1. GP acknowledges the support of the grants I2760-B30 from the Austrian Science Fund (FWF), BioTechMed-Graz Flagship award ILearnHeart, and MedalCare 18HLT07 from the EU.

Supplementary material

Supplementary material containing detailed numerical settings to enable replication of simulation results with openCARP is available online.

Supplemental video 1: Induced VT within Pig 3 model using VITA. Transmembrane voltage (V_m) of the reentrant wave in the high resolution (same scale as Fig. 9). V_m and other state variables were mapped from the down-sampled (R-E) onto the high resolution (R-D) model.

Supplemental video 2: Induced VT within Pig 3 model using VARP. Conduction block and reentry following a premature S2 beat delivered near the base of the LV model. Transmembrane voltage (V_m) of the premature S2 (coupling interval of 250 ms) that blocked at the isthmus and degenerated into reentry (same scale as Fig. 9).

Supplemental video 3: Induced VT within Pig 4 model using VARP. Functional block and reentry following a premature S2 beat delivered at a mid point between the apex and base of the LV model. Transmembrane voltage (V_m) of the premature S2 (coupling interval of 250 ms) that blocked at infarct BZ and degenerated into reentry (same scale as Fig. 10).

Supplementary material associated with this article can be found, in the online version, at doi:[10.1016/j.media.2022.102483](https://doi.org/10.1016/j.media.2022.102483)

References

- Aliot, E.M., Stevenson, W.G., Almendral-Garrote, J.M., Bogun, F., Calkins, C.H., Delacretaz, E., Della Bella, P., Hindricks, G., Jaïs, P., Josephson, M.E., Kautzner, J., Kay, G.N., Kuck, K.H., Lerman, B.B., Marchlinski, F., Reddy, V., Schalij, M.J., Schilling, R., Soejima, K., Wilber, D., 2009. European heart rhythm association (EHRA); registered branch of the european society of cardiology (ESC); heart rhythm society (HRS); american college of cardiology (ACC); american heart association (AHA). EHRA/HRS expert consensus on catheter ablation of ventricular arrhythmias: developed in a partnership with the european heart rhythm association (EHRA), a registered branch of the european society of cardiology (ESC), and the heart rhythm society (HRS); in collaboration with the american college of cardiology (ACC) and the american heart association (AHA). *Heart Rhythm* 6 (6), 886–933.
- Arevalo, H., Plank, G., Helm, P., Halperin, H., Trayanova, N., 2013. Tachycardia in post-infarction hearts: insights from 3d image-based ventricular models. *PLoS ONE* 8 (7), e68872.
- Arevalo, H.J., Vadakkumpadan, F., Guallar, E., Jebb, A., Malamas, P., Wu, K.C., Trayanova, N.A., 2016. Arrhythmia risk stratification of patients after myocardial infarction using personalized heart models. *Nat. Commun.* 7, 11437.
- Ashikaga, H., Arevalo, H., Vadakkumpadan, F., Blake, R.C., Bayer, J.D., Nazarian, S., Muz Zviman, M., Tandri, H., Berger, R.D., Calkins, H., Herzka, D.A., Trayanova, N.A., Halperin, H.R., 2013. Feasibility of image-based simulation to estimate ablation target in human ventricular arrhythmia. *Heart Rhythm* 10 (8), 1109–1116.
- Bayer, J.D., Blake, R.C., Plank, G., Trayanova, N.A., 2012. A novel rule-based algorithm for assigning myocardial fiber orientation to computational heart models. *Ann. Biomed. Eng.* 40 (10), 2243–2254.
- Berrueto, A., Fernández-Armenta, J., Andreu, D., Penela, D., Herczku, C., Evertz, R., Cipolletta, L., Acosta, J., Borrás, R., Arbelo, E., Tolosana, J.M., Brugada, J., Mont, L., 2015. Scar dechanneling: new method for scar-related left ventricular tachycardia substrate ablation. *Circ. Arrhythm. Electrophysiol.* 8 (2), 326–336.
- Bishop, M.J., Plank, G., 2010. Representing cardiac bidomain bath-loading effects by an augmented monodomain approach: application to complex ventricular models. *IEEE Trans. Biomed. Eng.* 58, 1066–1075.
- Boyle, P.M., Zghaib, T., Zahid, S., Ali, R.L., Deng, D., Franceschi, W.H., Hakim, J.B., Murphy, M.J., Prakosa, A., Zimmerman, S.L., Ashikaga, H., Marine, J.E., Kolandaivelu, A., Nazarian, S., Spragg, D.D., Calkins, H., Trayanova, N.A., 2019. Computationally guided personalized targeted ablation of persistent atrial fibrillation. *Nat. Biomed. Eng.* 11, 870–879.
- Campos, F.O., Orini, M., Arnold, R., Whitaker, J., O'Neill, M., Razavi, R., Plank, G., Hanson, B., Porter, B., Rinaldi, C.A., Gill, J., Lambiase, P.D., Taggart, P., Bishop, M.J., 2021. Assessing the ability of substrate mapping techniques to guide ventricular tachycardia ablation using computational modelling. *Comput. Biol. Med.* 130, 104214.

- Campos, F.O., Whitaker, J., Neji, R., Roujol, S., O'Neill, M., Plank, G., Bishop, M.J., 2019. Factors promoting conduction slowing as substrates for block and reentry in infarcted hearts. *Biophys. J.* 117 (12), 2361–2374.
- Campos, J.O., Oliveira, R.S., dos Santos, R.W., Rocha, B.M., 2016. Lattice boltzmann method for parallel simulations of cardiac electrophysiology using GPUs. *J. Comput. Appl. Math.* 295, 70–82.
- Cedilnik, N., Duchateau, J., Dubois, R., Sacher, F., Jais, P., Cochet, H., Sermesant, M., 2018. Fast personalized electrophysiological models from computed tomography images for ventricular tachycardia ablation planning. *Europace* 20 (suppl3), iii94–iii101.
- Chen, Z., Cabrera-Lozoya, R., Relan, J., Sohal, M., Shetty, A., Karim, R., Delingette, H., Gill, J., Rhode, K., Ayache, N., Taggart, P., Rinaldi, C.A., Sermesant, M., Razavi, R., 2016. Biophysical modeling predicts ventricular tachycardia inducibility and circuit morphology: a combined clinical validation and computer modeling approach. *J. Cardiovasc. Electrophysiol.* 27 (7), 851–860.
- Ciaccio, E.J., Anter, E., Coromilas, J., Wan, E.Y., Yarmohammadi, H., Wit, A.L., Peters, N.S., Garan, H., 2021. Structure and function of the ventricular tachycardia isthmus. *Heart Rhythm*. S1547–5271(21)01999–8
- Colli Franzone, P., Guerri, L., Rovida, S., 1990. Wavefront propagation in an activation model of the anisotropic cardiac tissue: asymptotic analysis and numerical simulations. *J. Math. Biol.* 28 (2), 121–176.
- Coronel, R., Wilms-Schopman, F.J., Ophof, T., Janse, M.J., 2009. Dispersion of repolarization and arrhythmogenesis. *Heart Rhythm* 6 (4), 537–543.
- Costa, C.M., Campos, F.O., Prassl, A.J., dos Santos, R.W., Sánchez-Quintana, D., Hofer, H.A.E., Plank, G., 2014. An efficient finite element approach for modeling fibrotic clefts in the heart. *IEEE Trans. Biomed. Eng.* 61 (3), 900–910.
- Costa, C.M., Hoetzl, E., Rocha, B.M., Prassl, A.J., Plank, G., 2013. Automatic parameterization strategy for cardiac electrophysiology simulations. *Comput. Cardiol.* 40, 373–376.
- Crozier, A., Augustin, C.M., Neic, A., Prassl, A.J., Holler, M., Fastl, T.E., Hennemuth, A., Bredies, K., Kuehne, T., Bishop, M.J., Niederer, S.A., Plank, G., 2016. Image-based personalization of cardiac anatomy for coupled electromechanical modeling. *Ann. Biomed. Eng.* 44 (1), 58–70.
- Deng, D., Arevalo, H., Pashakhanloo, F., Prakosa, A., Ashikaga, H., McVeigh, E., Halperin, H., Trayanova, N., 2015. Accuracy of prediction of infarct-related arrhythmic circuits from image-based models reconstructed from low and high resolution MRI. *Front. Physiol.* 6, 282.
- Deng, D., Prakosa, A., Shade, J., Nikolov, P., Trayanova, N.A., 2019. Characterizing conduction channels in postinfarction patients using a personalized virtual heart. *Biophys. J.* 117 (12), 2287–2294.
- Deng, D., Prakosa, A., Shade, J., Nikolov, P., Trayanova, N.A., 2019. Sensitivity of ablation targets prediction to electrophysiological parameter variability in image-based computational models of ventricular tachycardia in post-infarction patients. *Front. Physiol.* 10, 628.
- El-Sherif, N., Boutjdir, M., Turitto, G., 2017. Sudden cardiac death in ischemic heart disease: pathophysiology and risk stratification. *Card Electrophysiol. Clin.* 9 (4), 681–691.
- Gillette, K., Gsell, M.A.F., Prassl, A.J., Karabelas, E., Reiter, U., Reiter, G., Grandits, T., Payer, C., Štern, D., Urschler, M., Bayer, J.D., Augustin, C.M., Neic, A., Pock, T., Vigmond, E.J., Plank, G., 2021. A framework for the generation of digital twins of cardiac electrophysiology from clinical 12-lead ECGs. *Med. Image Anal.* 71, 102080.
- Graham, A.J., Orini, M., Lambiase, P.D., 2017. Limitations and challenges in mapping ventricular tachycardia: new technologies and future directions. *Arrhythm. Electrophysiol. Rev.* 6 (3), 118–124.
- Hooks, D.A., Trew, M.L., Caldwell, B.J., Sands, G.B., LeGrice, I.J., Smaill, B.H., 2007. Laminar arrangement of ventricular myocytes influences electrical behavior of the heart. *Circ. Res.* 101 (10), 103–112.
- Jacquemet, V., 2012. An eikonal-diffusion solver and its application to the interpolation and the simulation of reentrant cardiac activations. *Comput. Method. Programs. Biomed.* 108 (2), 548–558.
- Karim, R., Housden, R.J., Balasubramaniam, M., Chen, Z., Perry, D., Uddin, A., Al-Beyatt, Y., Palkhi, E., Acheampong, P., Obom, S., Hennemuth, A., Lu, Y., Bai, W., Shi, W., Gao, Y., Peitgen, H.O., Radau, P., Razavi, R., Tannenbaum, A., Rueckert, D., Cates, J., Schaeffter, T., Peters, D., MacLeod, R., Rhode, K., 2013. Evaluation of current algorithms for segmentation of scar tissue from late gadolinium enhancement cardiovascular magnetic resonance of the left atrium: an open-access grand challenge. *J. Cardiovasc. Magn. Reson.* 15 (1), 105.
- Keener, J.P., 1991. An eikonal-curvature equation for action potential propagation in myocardium. *J. Math. Biol.* 29 (7), 629–651.
- Kléber, A.G., Rudy, Y., 2004. Basic mechanisms of cardiac impulse propagation and associated arrhythmias. *Physiol. Rev.* 84 (2), 431–488.
- Kong, W.F., Sharifov, N.O.F., Ideker, R.E., Smith, W.M., Fast, V.G., 2007. Optical measurements of intramural action potentials in isolated porcine hearts using optodes. *Heart Rhythm* 4 (11), 1430–1436.
- Koplan, B.A., Stevenson, W.G., 2009. Ventricular tachycardia and sudden cardiac death. *Mayo Clin. Proc.* 84 (3), 289–297.
- Lim, B., Kim, J., Hwang, M., Song, J.S., Lee, J.K., Yu, H.T., Kim, T.H., Uhm, J.S., Joung, B., Lee, M.H., Pak, H.N., 2020. In situ procedure for high-efficiency computational modeling of atrial fibrillation reflecting personal anatomy, fiber orientation, fibrosis, and electrophysiology. *Sci. Rep.* 10 (1), 2417.
- Lopez-Perez, A., Sebastian, R., Izquierdo, M., Ruiz, R., Bishop, M., Ferrero, J.M., 2019. Personalized cardiac computational models: from clinical data to simulation of infarct-related ventricular tachycardia. *Front. Physiol.* 10, 580.
- Luke, R.A., Saffitz, J.E., 1991. Remodeling of ventricular conduction pathways in healed canine infarct border zones. *J. Clin. Invest.* 87 (5), 1594–1602.
- Mendonca Costa, C., Gemmell, P., Elliott, M.K., Whitaker, J., Campos, F.O., Strocchi, M., Neic, A., Gillette, K., Vigmond, W., Plank, G., Razavi, R., O'Neill, M., Rinaldi, C.A., Bishop, M.J., 2022. Determining anatomical and electrophysiological detail requirements for computational ventricular models of porcine myocardial infarction. *Comput. Biol. Med.* 141, 105061.
- Mendonca Costa, C., Plank, G., Rinaldi, C.A., Niederer, S.A., Bishop, M.J., 2018. Modeling the electrophysiological properties of the infarct border zone. *Front. Physiol.* 9 (356).
- Milotta, G., Munoz, C., Kunze, K.P., Neji, R., Figliozzi, S., Chiribiri, A., Hajhosseiny, R., Masci, P.G., Prieto, C., Botnar, R.M., 2021. 3D whole-heart grey-blood late gadolinium enhancement cardiovascular magnetic resonance imaging. *J. Cardiovasc. Magn. Reson.* 23 (1), 62.
- Monaci, S., Gillette, K., Puyol-Antón, E., Rajani, R., Plank, G., King, A., Bishop, M., 2021. Automated localisation of focal ventricular tachycardia from simulated implanted device electrograms: a combined physics-AI approach. *Front. Physiol.*
- Neic, A., Campos, F.O., Prassl, A.J., Niederer, S.A., Bishop, M.J., Vigmond, E.J., Plank, G., 2017. Efficient computation of electrograms and ECGs in human whole heart simulations using a reaction-eikonal model. *J. Comput. Phys.* 1 (346), 91–211.
- Neic, A., Gsell, M.A.F., Karabelas, E., Prassl, A.J., Plank, G., 2020. Automating image-based mesh generation and manipulation tasks in cardiac modeling workflows using meshtool. *SoftwareX* 11, 100454.
- Neic, A., Liebmann, M., Hoetzl, E., Mitchell, L., Vigmond, E.J., Haase, G., Plank, G., 2012. Accelerating cardiac bidomain simulations using graphics processing units. *IEEE Trans. Biomed. Eng.* 59 (8), 2281–2290.
- Niederer, S., Mitchell, L., Smith, N., Plank, G., 2011. Simulating human cardiac electrophysiology on clinical time-scales. *Front. Physiol.* 2, 14.
- Nishimura, T., Upadhyay, G.A., Aziz, Z.A., Beaser, A.D., Shatz, D.Y., Nayak, H.M., Tung, R., 2021. Circuit determinants of ventricular tachycardia cycle length: characterization of fast and unstable human ventricular tachycardia. *Circulation* 143 (3), 212–226.
- Orini, M., Seraphim, A., Graham, A., Bhuv, A., Zacur, E., Kellman, P., Schilling, R., Hunter, R., Dhinoja, M., Finlay, M.C., Ahsan, S., Chow, A.W., Moon, J.C., Lambiase, P.D., Manisty, C., 2021. Detailed assessment of low-voltage zones localization by cardiac MRI in patients with implantable devices. *J. Am. Coll. Cardiol.* EP.
- Pashakhanloo, F., Herzka, D.A., Halperin, H., McVeigh, E.R., Trayanova, N.A., 2018. Role of 3-dimensional architecture of scar and surviving tissue in ventricular tachycardia. *Circ. Arrhythm. Electrophysiol.* 11 (6), e006131.
- Perez-David, E., Arenal, A., Rubio-Guivernau, J.L., del Castillo, R., Atea, L., Arbelo, E., Caballero, E., Celorrio, V., Datino, T., Gonzalez-Torrecilla, E., Atienza, F., Ledesma-Carbayo, M.J., Bermejo, J., Medina, A., Fernández-Avilés, F., 2011. Noninvasive identification of ventricular tachycardia-related conducting channels using contrast-enhanced magnetic resonance imaging in patients with chronic myocardial infarction: comparison of signal intensity scar mapping and endocardial voltage mapping. *J. Am. Coll. Cardiol.* 57 (2), 184–194.
- Plank, G., Liebmann, M., Weber dos Santos, R., Vigmond, E.J., Haase, G., 2007. Algebraic multigrid preconditioner for the cardiac bidomain model. *IEEE Trans. Biomed. Eng.* 54 (4), 585–596.
- Plank, G., Loewe, A., Neic, A., Augustin, C., Huang, Y.L., Gsell, M.A.F., Karabelas, E., Nothstein, M., Prassl, A.J., Sánchez, J., Seemann, G., Vigmond, E.J., 2021. The openCARP simulation environment for cardiac electrophysiology. *Comput. Method. Program. Biomed.* 208, 106223.
- Plonsey, R., Barr, R.C., 1998. *Bioelectricity: A quantitative approach* (3rd edition). Springer.
- Potse, M., 2018. Scalable and accurate ECG simulation for reaction-diffusion models of the human heart. *Front. Physiol.* 9, 370.
- Prakosa, A., Arevalo, H.J., Deng, D., Boyle, P.M., Nikolov, P.P., Ashikaga, H., Blauer, J.J.E., Ghafoori, E., Park, C.J., Blake, R.C., Han, F.T., MacLeod, R.S., Halperin, H.R., Callans, D.J., Ranjan, R., Chrispin, J., Nazarian, S., Trayanova, N.A., 2018. Personalized virtual-heart technology for guiding the ablation of infarct-related ventricular tachycardia. *Nat. Biomed. Eng.* 2 (10), 732–740.
- Prassl, A.J., Kicking, F., Ahammer, H., Grau, V., Schneider, J.E., Hofer, E., Vigmond, E.J., Trayanova, N.A., Plank, G., 2009. Automatically generated, anatomically accurate meshes for cardiac electrophysiology problems. *IEEE Trans. Biomed. Eng.* 56 (5), 1318–1330.
- Project, T.C., 2018. *CGAL User and reference manual, 4.12 CGAL Editorial Board*. <https://doc.cgal.org/4.12/Manual/packages.html>
- Ranjan, R., McGann, C.J., Jeong, E.K., Hong, K., Kholmovski, E.G., Blauer, J., Wilson, B.D., Marrouche, N.F., Kim, D., 2015. Wideband late gadolinium enhanced magnetic resonance imaging for imaging myocardial scar without image artefacts induced by implantable cardioverter-defibrillator: a feasibility study at 3 t. *Europace* 17 (3), 483–488.
- Rashid, S., Rapacchi, S., Shivkumar, K., Plotnik, A., Finn, J.P., Hu, P., 2016. Modified wideband three-dimensional late gadolinium enhancement MRI for patients with implantable cardiac devices. *Magn. Reson. Med.* 75 (2), 572–584.
- Rashid, S., Rapacchi, S., Vaseghi, M., Tung, R., Shivkumar, K., Finn, J.P., Hu, P., 2014. Improved late gadolinium enhancement MR imaging for patients with implanted cardiac devices. *Radiology* 270 (1), 269–274.
- Razeghi, O., Sim, I., Roney, C.H., Karim, R., Chubb, H., Whitaker, J., O'Neill, L., Mukherjee, R., Wright, M., O'Neill, M., Williams, S.E., Niederer, S., 2020. Fully automatic atrial fibrosis assessment using a multilabel convolutional neural network. *Circ. Cardiovasc. Imaging* 13 (12), e011512.
- Relan, J., Chinchapatnam, P., Sermesant, M., Rhode, K., Ginks, M., Delingette, H., Rinaldi, C.A., Razavi, R., Ayache, N., 2011. Coupled personalization of cardiac electrophysiology models for prediction of ischaemic ventricular tachycardia. *Interface Focus* 1 (3), 396–407.

- Rocha, B.M., Campos, F.O., Amorim, R.M., Plank, G., dos Santos, R.W., Liebmann, M., Haase, G., 2011. Accelerating cardiac excitation spread simulations using graphics processing units. *Concurrency Comput.: Pract Exper* 23 (7), 708–720.
- Sánchez-Somonte, P., Quinto, L., Garre, P., Zaraket, F., Alarcón, F., Borràs, R., Caixal, G., Vázquez, S., Prat, S., Ortiz-Perez, J.T., Perea, R.J., Guasch, E., Tolosana, J.M., Berruezo, A., Arbelo, E., Sitges, M., Mont, L., Roca-Luque, I., 2021. Scar channels in cardiac magnetic resonance to predict appropriate therapies in primary prevention. *Heart Rhythm*. S1547–5271(21)00355–6
- dos Santos, R.W., Plank, G., Bauer, S., Vigmond, E.J., 2004. Parallel multigrid preconditioner for the cardiac bidomain model. *IEEE Trans. Biomed. Eng.* 51 (11), 1960–1968.
- Stevenson, W.G., 2009. Ventricular scars and ventricular tachycardia. *Trans. Am. Clin. Climatol. Assoc.* 120, 403–412.
- Stevenson, W.G., 2013. Current treatment of ventricular arrhythmias: state of the art. *Heart Rhythm* 10 (12), 1919–1926.
- Tanawattiwat, T., Nazarian, S., Calkins, H., 2016. The role of catheter ablation in the management of ventricular tachycardia. *Eur. Heart J.* 37 (7), 594–609.
- ten Tusscher, K.H., Panfilov, A.V., 2006. Alternans and spiral breakup in a human ventricular tissue model. *Am. J. Physiol. Heart Circ. Physiol.* 291 (3), H1088–H1100.
- Vasconcellos, E.C., Clua, E.W.G., Fenton, F.H., Zamith, M., 2020. Accelerating simulations of cardiac electrical dynamics through a multi-GPU platform and an optimized data structure. *Concurr. Comput.* 32 (5), e5528.
- Vigmond, E., Hughes, M., Plank, G., Leon, L., 2003. Computational tools for modeling electrical activity in cardiac tissue. *J. Electrocardiol.* 36 Suppl, 69–74.
- Vigmond, E.J., Weber dos Santos, R., Prassl, A.J., Deo, M., Plank, G., 2008. Solvers for the cardiac bidomain equations. *Prog. Biophys. Mol. Biol.* 96 (1–3), 3–18.
- Volosin, K.J., Beauregard, L.A., Fabiszewski, R., Mattingly, H., Waxman, H.L., 1991. Spontaneous changes in ventricular tachycardia cycle length. *J. Am. Coll. Cardiol.* 17 (2), 409–414.
- Whitaker, J., Neji, R., Byrne, N., Puyol-Antón, E., Mukherjee, R.K., Williams, S.E., Chubb, H., O'Neill, L., Razeghi, O., Connolly, A., Rhode, K., Niederer, S., King, A., Tschabrunn, C., Anter, E., Nezafat, R., Bishop, M.J., O'Neill, M., Razavi, R., Roujol, S., 2019. Improved co-registration of ex-vivo and in-vivo cardiovascular magnetic resonance images using heart-specific flexible 3d printed acrylic scaffold combined with non-rigid registration. *J. Cardiovasc. Magn. Reson.* 10 (21(1)), 62.
- Willems, S., Tiltz, R.R., Steven, D., Kääh, S., Wegscheider, K., Gellèr, L., Meyer, C., Heeger, C.H., Metzner, A., Sinner, M.F., Schlüter, M., Nordbeck, P., Eckardt, L., Bogossian, H., Sultan, A., Wenzel, B., Kuck, K.H., 2020. Preventive or deferred ablation of ventricular tachycardia in patients with ischemic cardiomyopathy and implantable defibrillator (BERLIN VT): a multicenter randomized trial. *Circulation* 141 (13), 1057–1067.
- Wissner, E., Stevenson, W.G., Kuck, K.H., 2012. Catheter ablation of ventricular tachycardia in ischaemic and non-ischaemic cardiomyopathy: where are we today? a clinical review. *Eur. Heart J.* 33 (12), 1440–1450.
- Yamashita, S., Sacher, F., Hooks, D.A., Berte, B., Sellal, J.M., Frontera, A., Jefairi, N.A., Komatsu, Y., Amraoui, S., Denis, A., Derval, N., Sermesant, M., Laurent, F., Montaudon, M., Hocini, M., Haïssaguerre, M., Jaïs, P., Cochet, H., 2016. Myocardial wall thinning predicts transmural substrate in patients with scar-related ventricular tachycardia. *Heart Rhythm* 14 (2), 155–163.
- Zahid, S., Whyte, K.N., Schwarz, E.L., Blake, R.C., Boyle, P.M., Chrispin, J., Prakosa, A., Ipek, E.G., Pashakhanloo, F., Halperin, H.R., Calkins, H., Berger, R.D., Nazarian, S., Trayanova, N.A., 2016. Feasibility of using patient-specific models and the “minimum cut” algorithm to predict optimal ablation targets for left atrial flutter. *Heart Rhythm* 13 (8), 1687–1698.